Garnierite characterisation for open data bases for nickel laterite exploration

Nicolas Maubec, Beate Orberger, P.G. Blaineau, C. Villanova-De-Benavent, Anthony da Silva Alves, Cédric Duée, Guillaume Wille, Sylvain Delchini

Garnierite characterization for open mineral databases

Maubec, N.[1*], Orberger, B.[2/3], Blaineau, PG.[1/4], Villanova-de-Benavent, C.[5], Da Silva Alves, A.[1/3], Duée, C.[1], Wille, G.[1], Delchini, S.[1]

1. BRGM, Orléans, France; n.maubec@brgm.fr
2. GEOPS-Université Paris Saclay, Bât 504, 91405 ORSAY Cedex, France; beate.orberger@universite-paris-saclay.fr
3. Catura Geoprojects, 2 rue Marie Davy, 75014 Paris, France; beate.orberger@catura.eu
4. Université Poitiers, France
5. Facultat de Ciències de la Terra, Universitat de Barcelona, Martí i Franquès s/n, 08028 Barcelona, Spain; cvillanovadb@ub.edu

*Corresponding author:
Nicolas Maubec
n.maubec@brgm.fr
+33 2 38 64 31 45
BRGM – 3 avenue Claude Guillemin 45060 ORLEANS Cedex FRANCE

Abstract

The nickel laterite mining industry faces lower recovery rates related to low ore grades, multiple nickel carrying minerals, as well as lateral and vertical heterogeneities at ore deposit scale. Garnierite, a complex mixture of nickel-bearing phyllosilicates, occurs at the base of nickel laterite profiles. Samples of Ni-rich and Ni-poor phyllosilicates from garnierite and host saprolite, from New Caledonia and the Dominican Republic, were analyzed by laboratory X-ray diffractometry (XRD), Fourier Transform Infrared (FTIR) and Raman spectroscopies. These phyllosilicates are mainly composed of serpentine-, talc- and/or sepiolite-like phases. XRD allows clearly distinguishing the different phyllosilicate phases. Moreover, it shows a difference between Ni-rich and Ni-poor phases after refinement of the

diffractograms, in particular the (060) reflection, little exploited at present. When Ni is present, the peaks are broader and the spacing corresponding to the (060) reflection tends to be less than 1.534 Å. Mg substitution by Ni also cause shifts of hydroxyl bands in FTIR (3500-3800 cm^{-1} and 500-800 cm^{-1} spectral range), and Raman spectra (3500-3700 cm^{-1} spectral range). Moreover, the intensities of the bands can be correlated with the Ni content. Both are reliable indicators to define the nature of garnierite. In Raman spectroscopy, the substitution of Mg by Ni generates shifts on most bands, and there is a variation in intensity ratios between several bands which are correlated with Ni content.

Our results can be applied to spectra obtained by online and handheld analytical devices, in-field core scanners or XRD/X-Ray fluorescence (XRF) combined expert systems.

Keywords: Garnierite; Mg/Ni substitution; X-Ray diffraction; FTIR; Raman spectroscopy

1. Introduction

Nickel (Ni) laterites represent about 70% of the Ni resources worldwide (e.g. Butt and Cluzel, 2013; Dalvi et al. 2004; Gleeson et al. 2003), but only about 60 % of the world's production is provided by Ni laterites (McRae, 2021). One of the reasons is the low recovery rate during ore processing, in particular of the "hydrous Mg silicate" and the "clay" type Ni laterites. These ores are composed of Ni-rich and Ni-poor serpentine, swelling and non-swelling clay minerals, and hydrotalcites in part poorly crystalline, and occur in the lower part of the laterite profile. However, these phases can host up to 27% of Ni (Bish and Brindley, 1977; Brindley, 1980; Freyssinet et al. 2005; Cathelineau et al. 2016; Fritsch et al. 2016; Putzolu et al. 2018; Putzolu et al. 2021; Tauler et al. 2017; Villanova-de-Benavent et al. 2014).

The Ni-rich phyllosilicates occur disseminated in the saprolite matrix, concentrated as fracture and vein infillings in the upper part of the serpentinized peridotites and the saprock, or, to a lesser extent (e.g. Tiebaghi), in porous silica rocks containing serpentinite clasts (Duée et al. 2019; El Mendili et al. 2020; Pelletier, 1983; Secchi et al. 2018, Cluzel and Vigier, 2008). Garnierite, a mixture of nanocrystallites of crystalline serpentine, talc, chlorite, sepiolite and/or smectite, occurring in fractures, is the main Ni ore (Brindley and Hang, 1973; Fritsch et al. 2016; Villanova-de-Benavent et al. 2016; Wells et al. 2009). It was defined by Jules Garnier (1867) in New Caledonia. The garnierite terminology is not recognized by the International Mineralogical Association (IMA), as its mineralogical composition and colors (whitish, greenish to green-blue) vary according to the evolution of the ore deposit. Garnierite can be collomorphous, poorly crystalline or amorphous (e.g. Cluzel and Vigier, 2008). These phases have been widely studied by laboratory analyses such as XRD, FTIR, and Raman spectroscopy in order to distinguish those enriched in Ni (Bosio et al. 1975; Cathelineau et al. 2015; Decarreau et al. 1987; Mano et al. 2014; Villanova-de-Benavent et al. 2019). Some studies identify or classify the garnierite forming minerals according to their structure and their basal spacings, determined by XRD (Brindley, 1980; Brindley et al. 1977, 1979; Wells et al. 2009). It was proposed to distinguished serpentine-like phases (1:1 layer type minerals - 7 Å), which include lizardite-népouite and chrysotile-pecoraite series; talc-like phases (2:1 layer type minerals - 10 Å), which include talc-willemseite and kerolite-pimelite series; and sepiolite-like phases (2:1 layer type minerals - 12 Å), which consist in sepiolite-falcondoite series. More details about the nomenclature can be found in the study of Brindley (1980).

At present, mining companies seek to automatize drill core logging using drill core scanners composed of sensors accessing chemistry and mineralogy. These instruments are on the market (e e.g. Corescanner™, https://corescan.com.au/; Minalyzer CS™,

https://minalyze.com/; Avaatech XRF core scanner, https://www.avaatech.com; Terracore, http://terracoregeo.com) or in pre-industrial state (e.g. SOLSA, www.solsa-mining.eu, RTM mining, EIT-KIC ANCORELOG, EIT-KIC T-REX). In the SOLSA project, a combined benchtop XRF-XRD-Raman instrument was developed, measuring powdered samples on mine sites. All these devices contribute to more efficient mining and processing through smart interpretation of the collected data. Hence, operational exploration and processing costs, representing about 70% of a mining project, can be significantly reduced.

However, the efficiency of in-field measurements and data interpretation are highly dependent on ore- deposit adapted databases.

Apart from Ni, these laterites may also host economic grades of cobalt (Co) and scandium (Sc) (Anawati et al. 2020; Chassé et al. 2016, 2019; Kaya and Topkaya, 2016; Marsch et al. 2011; Orberger & Van den Ent, 2019; Putzolu et al. 2019; Teitler et al. 2019; Williams-Jones and Vasyukova, 2018; Yongue-Fouateu et al. 2006). Contained in various silicates and oxy-hydroxides, Co and Sc can be more efficiently extracted when systematic, reliable, at least semi-quantitative, chemical and mineralogical data are smartly interpreted.

For mining companies, the precise determination of the mineralogy and the mineral chemistry of the ores is crucial. For unambiguous identification of the complex phases, solid and robust open databases are indispensable (Raman Open Database, El Mendili et al. 2019; COD, Grazulis et al. 2009, 2012, Hyperspectral Open Database-(HOD) as part of the SOLSA project).

The goal of this paper is the specific evaluation of XRD, FTIR and Raman data on garnierites. In this line, we present a comprehensive mineralogical study of three garnierite samples from New Caledonia, and of two garnierite samples from the Dominican Republic, the latter previously studied in Villanova-de-Benavent et al. (2014, 2016, 2019). All samples have been

analyzed by electron probe micro-analysis (EMPA), X-ray diffraction (XRD), Fourier Transform Infrared and Raman spectroscopy. These data can be used to calibrate combined XRF-XRD benchtop systems.

2. Materials and methods

2.1. Samples

A set of garnierite samples, representative of different Ni laterite facies and mineralogy, were investigated. Three samples, (NC1 to NC3), are from New Caledonia (Fig. 1 a-c) come from the garnierite collection at BRGM set-up from numerous field campaigns and from ERAMET-SLN. Two samples consist of breccias hosting saprolite clasts (dark, grey brown) and garnierite veins, dark green for NC1, and blue-green for NC2. (Fig. 1a,b). The third sample from New Caledonia (NC3) is composed of a blue-green "garnierite" matrix in contact with saprolite (Fig. 1c).

Samples DR1 and DR2 are from the Falcondo mining district in the Dominican Republic, and were described in Tauler et al. (2009) and Villanova-de-Benavent et al. (2014, 2016, 2019). Sample DR1 features bright green garnierite fragments cemented by garnierite, while sample DR2 consists of pale greenish bundles of fibers.

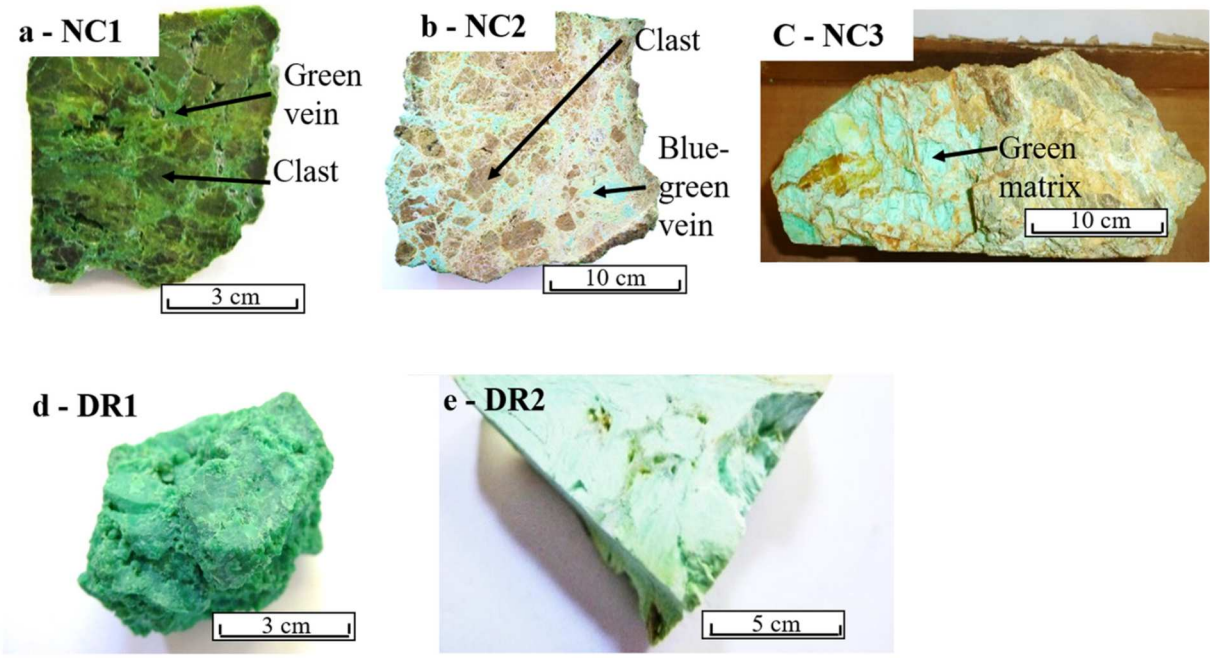

Figure 1. Selected samples from New Caledonia (NC1 to NC3) and from the Dominican Republic (DR1 to DR2), showing the areas sampled for this study.

2.2. Sample preparation

The samples were analyzed by EPMA, XRD, FTIR and micro-Raman spectroscopy.

XRD and FTIR analyses were carried out on powders. Due to the heterogeneity of the samples, it was decided to handpick a few tens of milligrams from selected areas of each sample, in order to study the most homogeneous phases. For NC1, samples were taken from a saprolite clast (NC1_clast) and from the veins surrounding these clasts (NC1_green vein). For NC2, samples were taken on the saprolite clasts (NC2_clast) and the blue-green veins around the clasts (NC2_blue_green vein). For NC3, only the greenish part (NC3_green matrix) was sampled. For DR1 and DR2, more homogeneous, only garnierite parts were sampled. The samples were ground in an agate mortar and sieved at 63 µm.

Raman spectroscopy and EPMA were performed on polished thin sections on the areas of interest.

147 2.3. Analytical methods

148 2.3.1. Electron Probe Micro-Analysis (EPMA)

149 Quantitative electron probe microanalyses were performed with a CAMECA SX FIVE
150 electron microprobe equipped with five vertical wavelength dispersive spectrometers (WDS).
151 The analyses were performed on carbon-coated (20–30 nm) polished thin sections using a 15
152 kV acceleration voltage, 20 nA probe current and 1-2 µm spot size. The system was calibrated
153 with albite for Na (Kα), periclase for Mg (Kα), Al_2O_3 for Al (Kα), andradite for Si and Ca
154 (Kα), orthoclase for K (Kα), $MnTiO_3$ for Mn and Ti (Kα), Fe_2O_3 for Fe (Kα), Cr_2O_3 for Cr
155 (Kα), NiO for Ni (Kα) and CoO for Co (Kα). Matrix corrections were performed with the
156 PAP computing programs of Pouchou and Pichoir (1984). For each sample, the chemical
157 composition was obtained from about ten measurements on average (varying from 9 to 19
158 measurements depending on the sample). These point analyses were acquired in areas of a
159 few square millimeters. Considering the small particle size (submicrometric) of the
160 phyllosilicates, the results give an average chemical composition that may correspond to the
161 analysis of one or more mineral phases. The structural formulae of serpentine and serpentine-
162 like minerals were calculated on the basis of 7 oxygens. For talc- and sepiolite-like phases,
163 calculations were performed using 11 and 32 oxygens, respectively.

164

165 2.3.2. X-ray diffractometry (XRD)

166 XRD analyses were performed on randomly oriented samples. For each sample, some tens of
167 milligrams of powders were set on a zero-background sample holder. The diffractograms
168 were acquired with a Bruker D8 Advance DA VINCI diffractometer equipped with a CuKα
169 source (λ = 1.5406 Å), operating at 40kV and 40mA, and a LYNXEYE XE 1D detector with
170 a 3.3° opening. The XRD patterns were collected in continuous scan mode over the 4-

75°2θ range with a step size and a measuring time of 0.03°2θ and 576 seconds per step, respectively.

As the position of the (060) reflection can be related to the Ni content in clay minerals (Baron and Petit, 2016), a specific study of this reflection was carried out by recording a diffractogram over the range 57-64°2θ, with a step of 0.03°2θ and a counting time of 576 seconds per step. The position of the (060) reflection and the full width half maximum (FWHM) of (001) and (060) reflections were determined by fitting XRD patterns with a fundamental parameter approach in the TOPAS V.6 and DIFFRAC.EVA softwares (Bruker, 2017).

2.3.3. Fourier Transform Infrared spectroscopy (FTIR)

FTIR spectra were obtained using a Bruker Equinox 55 FTIR spectrometer, equipped with a middle-infrared (MIR) source and a KBr beam splitter. For each sample, 30 scans in the 4000-400 cm^{-1} spectral range were recorded with a resolution of 4 cm^{-1}. The analyses were carried out on pellet discs consisting of a mixture of 0.5 mg of sample and 150 mg of KBr. The diameter of the pellets is 13 mm. Prior to analyses, the pellets were stored at 60°C to minimize the absorption of water by KBr and by the sample.

2.3.4. Micro-Raman spectroscopy

Raman measurements were performed with a Renishaw InVIA Reflex microspectrometer, coupled to a DMLM Leica microscope, equipped with Renishaw *WiRE*™ software. Three different lasers were used (λ0 = 514.5 nm; 633 nm and 785 nm). The analyses were carried out on polished thin sections using the 50x or 100x objective (NA = 0.90), with a laser power of around 1 mW at the sample surface. The Raman spectrometer was used in continuous

scanning mode with large spectral windows from 100 to 4000 cm^{-1}. Acquisition times (generally over 10 seconds) and accumulations of spectra vary depending on the mineral type.

3. Results

3.1. Mineral chemistry (EPMA)

The average chemical compositions with the corresponding structural formulae are given in the table 1. The ternary diagram Si-Ni-(Mg+Fe) provides initial information on the nature of the minerals that constitute each sample (Figure 2). Thus, it appears that the clasts present compositions close to the Mg-rich serpentines. On average, these samples contain less than 10 wt.% of NiO and between 2 and 6 wt.% of FeO. The (Ni/(Ni+Mg) ratio, which corresponds to Mg/Ni substitution rate, is 27% and 14% in NC1_clast and NC2_clast, respectively. The average structural formulae of these samples are close to the theoretical composition of a serpentine ($Mg_3Si_2O_5(OH)_4$). For the clasts, the number of tetrahedral cations is between 1.95 and 2.05 and the octahedral occupancy is between 2.9 and 3.1. These results are similar to those reported for samples from Indonesia (Golightly and Arancibia, 1979) and New Caledonia (Manceau et al. 1985).

The composition of the garnierite veins from NC1 sample tends towards a Ni-rich serpentine. This sample contains 50 wt.% of NiO, and a Mg/Ni substitution rate of 97%. In addition, it is worth noting that NC1 garnierite veins are exceptionally rich in Co (0.56 wt.% of CoO), about 10 times higher in the veins than in the saprolite clasts (Table 1). The average structural formulae shows a slight excess of Si in tetrahedral sites (2.086) and a deficiency of octahedral cations (2.824). Similar observations are reported in various studies of serpentine-like garnierite (Brindley and Wan, 1975; Manceau et al. 1985; Villanova-de-Benavent et al. 2014; Wells et al. 2009).

In contrast, garnierite from the NC2 sample has a composition close to that of kerolite (talc-like). This sample contains 9 wt.% of NiO, similarly to the clast of the NC1, but twofold higher than the clasts from NC2. The structural formula shows that the number of tetrahedral cations is slightly deficient (3.898 instead of 4) in the ideal formula of talc $Mg_3Si_4O_{10}(OH)_2$). In contrast, the number of cations in octahedral sites is in excess (3.207). The deviation from the ideal formula is similar to those reported in previous studies (Brindley et al. 1979; Brindley and Hang, 1973; Manceau et al. 1985; Villanova-de-Benavent et al. 2014, Wells et al. 2009).

Among the other garnierites, sample NC3 also has a talc-like composition, but with a higher Ni content than the garnierite in the NC2 sample. Its Mg/Ni substitution rate is 55% compared to 33% in NC2_blue green vein. The number of cations in tetrahedral and octahedral sites is equivalent to the one from NC2_blue green vein.

The average chemical composition of the DR1 sample shows that it is Ni-rich. Its Mg/Ni substitution rate is 91%. The distribution of the analysis points in the ternary diagram does not allow defining a typical mineralogy. This sample probably consists of a mixture of minerals, including serpentines and talc-like minerals. Therefore, for this sample, the structural formulae were calculated assuming 7 and 11 oxygens (Wells et al. 2009). On the basis of 7 oxygens, the results show a deviation from the ideal formula of a serpentine. There is an excess of cations in the tetrahedral site (2.314 instead of 2) and a strong deficit in octahedral cations (2.373 instead of 3). In contrast, the calculation based of 11 oxygens shows that the number of tetrahedral cations is in deficit, while it is largely in excess in octahedral sites.

The DR2 sample has a chemical composition corresponding to that of sepiolite-falcondoite, with 17.45 wt.% of NiO and an average Mg/Ni substitution rate of 62%. Its average structural formula shows a minor deviation from the ideal formula of sepiolite ($Mg_8Si_{12}O_{30}(OH)_4.12H_2O$).

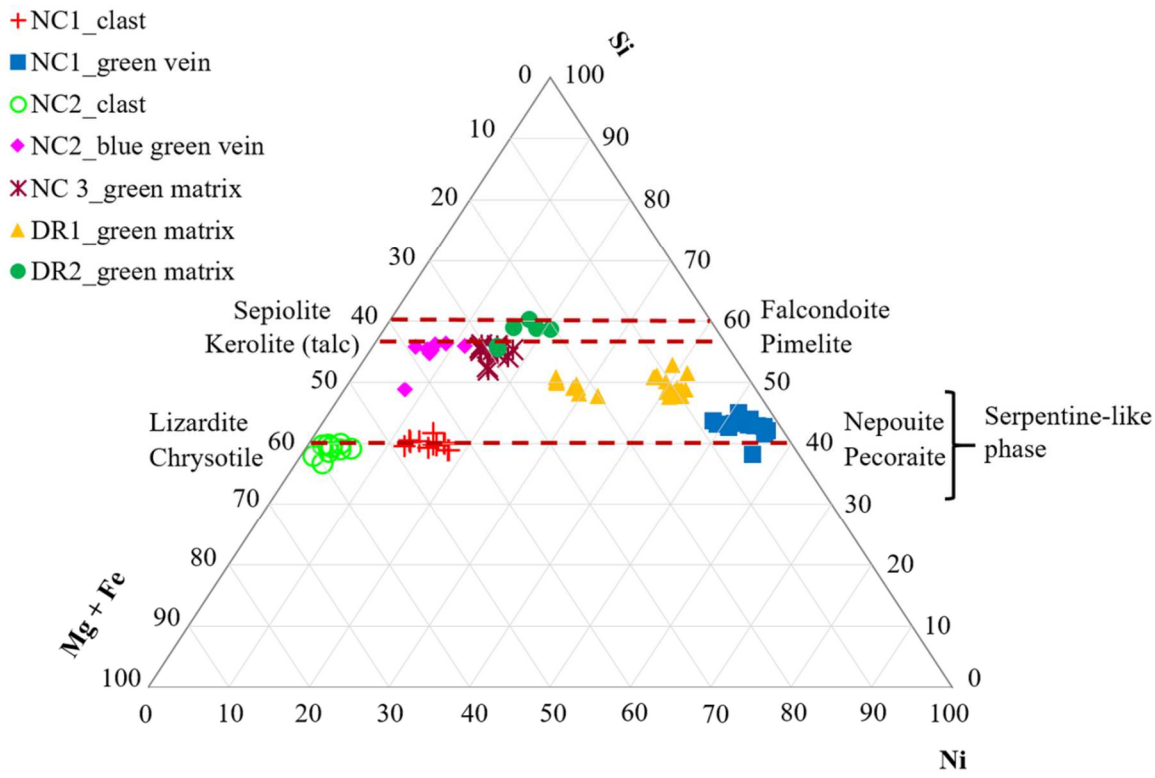

Figure 2. Ternary diagram Si–Ni–(Mg+Fe) (atomic proportions) showing the chemical compositions of the clasts and garnierites.

Table 1. Average composition (average of about 10 point analyses each) and structural formulae of the studied clasts and garnierites. Av: average; σ: standard deviation; Tetr.: tetrahedral site; Oct.: octahedral site.

Sample	NC1_Clast		NC1_green vein		NC2_Clast		NC2_green vein		NC3_green matrix		DR1_green matrix		DR2_green matrix	
Mineral type	Serpentine		Serpentine		Serpentine		Talc		Talc		Serpentine + talc		Sepiolite	
wt %	Av	σ	Av	σ	Av	σ	Av	σ	Av	σ	Av	σ	Av	σ
SiO_2	40.97	0.72	33.06	1.22	37.77	1.16	50.73	2.58	54.53	1.69	40.93	1.49	47.66	7.94
Al_2O_3	0.09	0.02	0.02	0.02	0.01	0.01	0.04	0.02	0.01	0.01	0.01	0.02	0.09	0.07
MgO	32.73	1.28	2.21	1.07	34.62	2.26	23.11	2.59	19.86	1.14	5.61	0.76	13.82	4.30
Cr_2O_3	0.02	0.04	0.03	0.02	0.00	0.00	0.00	0.01	0.00	0.01	0.00	0.01	0.00	0.01
MnO	0.05	0.04	0.01	0.03	0.05	0.05	0.03	0.03	0.00	0.00	0.01	0.02	0.01	0.02
FeO	2.41	0.18	0.10	0.13	5.62	1.33	0.14	0.24	0.00	0.00	0.11	0.09	0.01	0.02
CoO	0.11	0.02	0.56	0.21	0.03	0.03	0.01	0.01	0.01	0.02	0.02	0.04	0.00	0.00
NiO	9.34	1.37	50.84	2.92	4.17	1.54	8.91	1.50	18.97	1.70	41.68	1.20	17.45	2.20
Total	85.73	1.50	86.91	2.60	82.32	2.76	83.06	3.78	93.52	0.73	88.52	0.85	79.17	13.75
Ni/(Ni+Mg) %	27		97		14		33		55		91		62	
Si	2.040		2.086		1.954		3.894		3.896		2.313	3.634	11.719	
Al	0.005		0.001		0.001		0.004		0.001		0.001	0.001	0.026	
∑ Tetr.	2.045		2.087		1.955		3.898		3.897		2.314	3.635	11.745	
Mg	2.430		0.208		2.670		2.645		2.115		0.473	0.743	5.066	
Cr	0.001		0.001		0.000		0.000		0.000		0.000	0.000	0.000	
Mn	0.002		0.001		0.002		0.002		0.000		0.000	0.000	0.002	
Fe^{2+}	0.100		0.005		0.243		0.009		0.000		0.005	0.008	0.002	
Co	0.004		0.028		0.001		0.001		0.001		0.001	0.001	0.000	
Ni	0.374		2.581		0.174		0.550		1.090		1.894	2.977	3.452	
∑ Oct.	2.911		2.824		3.09		3.207		3.206		2.373	3.729	8.522	
Oxygens	7		7		7		11		11		7	11	32	

3.2. Mineralogy (XRD)

X-ray diffractograms are presented in Figures 3 and 4. They are serpentine-like, talc-like and sepiolite-like phases, characterized by main peaks located at 7.3 Å, 10.2 Å and 12.1 Å, respectively. The full width half maximum (FWHM) values of the (001) and (060) reflections are reported in table 2.

In the saprolite clasts (NC1-, and NC2-clasts), serpentine is a major component. This is in agreement with the chemical analyses (Figure 2). In sample NC2, this mineral is associated with quartz (26.6°2θ, 3.34 Å). This may explain a higher SiO_2 content in this sample than in the NC1-clast sample. It should also be noted that for both samples, a small amount of a talc-

like phase is detected, by a low intensity, broad peak centered at 10.2 Å. Although the two samples have a similar chemical and mineralogical composition, the study of the (060) reflection reveals a difference. The distance d_{060} is slightly longer in the sample NC2_clast (1.537 Å), than in sample NC1_clast (1.534 Å). Also, it appears that the peaks are slightly broader for NC1_clast than for NC2_clast. The FWHM of the 001 reflections are 0.430°2θ and 0.204°2θ, respectively (Table 2).

The garnierite veins of the NC1 sample are mainly composed of Ni-rich serpentine. In this sample, the serpentine-like phase is characterized by broader peaks (FWHM (001) = 0.897°2θ) and a shorter d_{060} distance (1.530 Å) compared to those observed in the saprolite clasts.

The garnierite veins of the NC2 sample are composed of a mixture of serpentine-, talc- and sepiolite-like phases and quartz. This composition is more complex than that expected from chemical analyses (kerolite–Mg-rich talc-like phase). The serpentine-like phase is defined by a narrow (FWHM (001) = 0.243°θ) and well-defined peak at 7.3 Å. Compared to the clasts and garnierite composed of Ni-rich serpentine, this characteristic indicates that the serpentine-like phase is rich in Mg. The peaks of the talc- and sepiolite-like phases are relatively broad and centered at 10.2 Å and 12 Å, respectively. Then, although this sample is composed of a mixture of phyllosilicates, the deconvolution of the (060) reflection does not allow distinguishing spacings corresponding to serpentine- or talc-like phases (for sepiolite, the (060) reflection is around 19.7°2θ, which corresponds to 4.50 Å). Only a peak corresponding to a spacing d_{060} of 1.527 Å has been defined. As the serpentine-like phase has similar characteristics to those of the clasts, one might expect to have a peak around 1.535 Å. However, this is not the case. The observation of a single peak at 1.527 Å may be related to a predominance of talc-like phase in the sample.

In sample NC3, the talc-like phase is predominant. This result is in agreement with the chemical analyses. The talc-like phase is defined by a broad basal peak at 10.2 Å and a (060) reflection centered at 1.529 Å. This reflection is close to the one from the garnierite veins of the NC2 sample.

The sample DR1 presents a mineralogy close to that observed for NC2 green vein sample. It is composed of a mixture of serpentine-, talc- and sepiolite-like phases associated with quartz. However, as indicated by the chemical analyses, this sample is much richer in Ni than the NC2 garnierite (Table 1). This results in a broad basal peak, which characterizes all phyllosilicates, in contrast to the garnierite of the sample NC2. It is possible that Ni is present in the structure of all the minerals that characterizes DR1.

As expected with the chemical analyses, the DR2 sample is composed solely of a sepiolite-like mineral. It is characterized by a main peak centered at 12.1 Å.

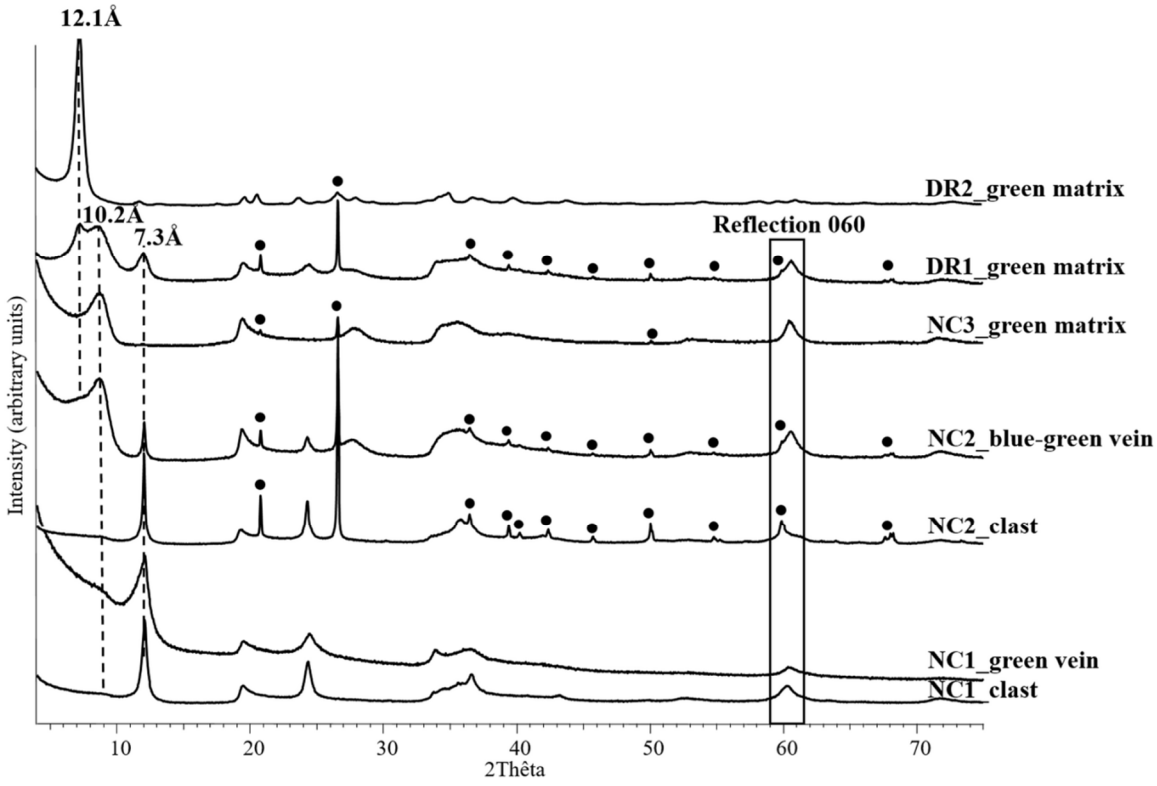

Figure 3. X-ray diffractograms of the samples selected for this study, with the main basal spacings of serpentine-like, talc-like and sepiolite-like phases at 7.3Å, 10.2Å and 12.1Å, respectively. Black circles correspond to quartz peaks.

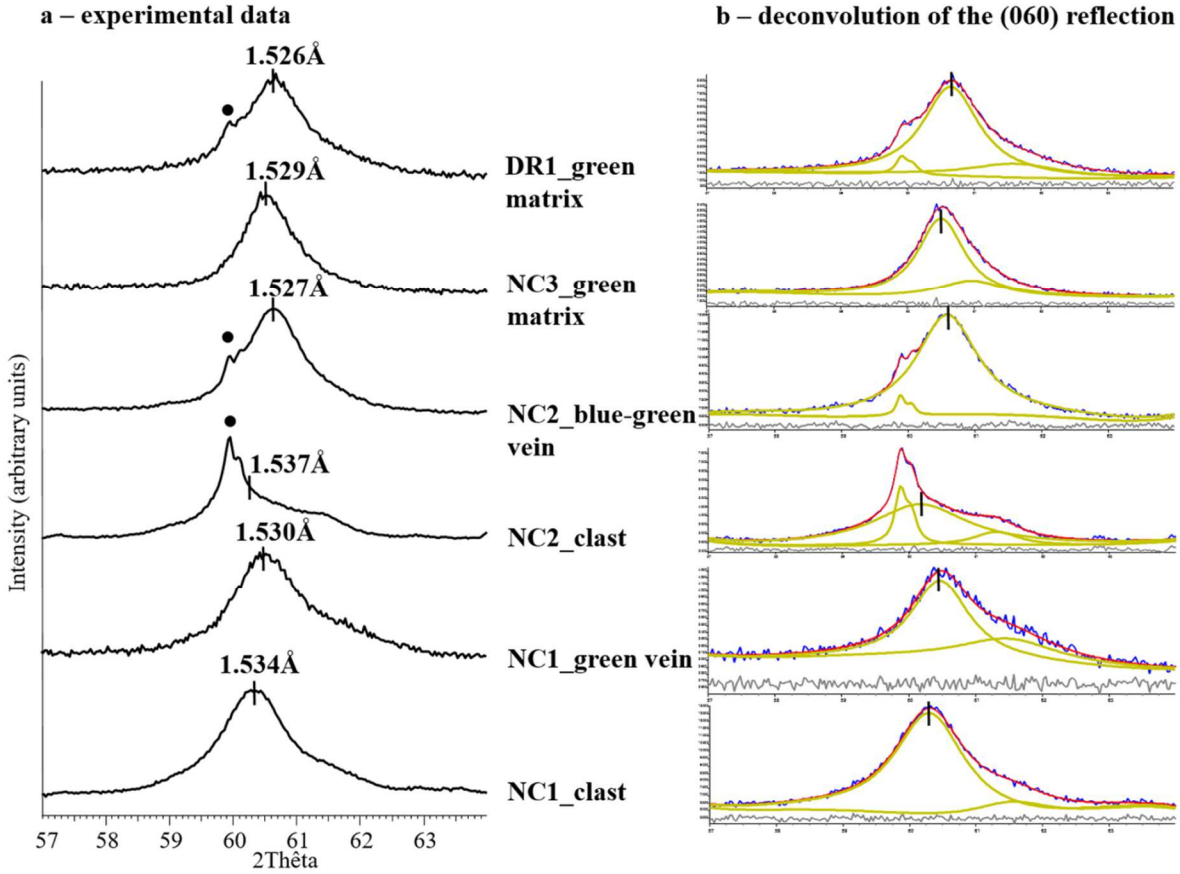

Figure 4. X-ray diffractograms of the (060) reflections of serpentine-like and talc-like phases present in NC1, NC2, NC3 and DR1 samples, and their profile refinement: experimental pattern in blue; calculated pattern in red; difference in grey.

Table 2. Full width half maximum (FWHM) values of the main reflections observed by XRD for the seven samples. The values are expressed in °2θ.

Sample	FWHM – (001) reflection			FWHM – (060) reflection
	12.1 Å	10.2 Å	7.3 Å	
NC1_clast	-	1.149	0.430	0.913
NC1_green vein	-	1.168	0.897	1.062
NC2_clast	-	0.834	0.204	0.729
NC2_blue green vein	1.703	1.347	0.243	1.086

NC3_green matrix	**-**	**1.345**	**-**	**0.931**
DR1_green matrix	**1.043**	**1.633**	**0.903**	**1.060**
DR2_green matrix	**0.700**	**-**	**-**	**-**

Table 3 summarizes the mineralogical characteristics obtained from XRD of the different types of minerals of this study. The three types of minerals (serpentine-like, talc-like and sepiolite-like) are highlighted by distinct basal distances located at 7.3 Å, 10.2 Å and 12.1 Å, respectively. In the case of serpentine, the shape of the peaks as well as the position of the d_{060} reflection are indicators of the presence of Ni within this type of phase. In the presence of Ni, the peaks are broader (FWHM (001) lower than 0.430°2θ for Ni-poor serpentine and close to 0.900°2θ for Ni-rich serpentine) and the distance corresponding to the (060) reflection tends to be less than 1.534 Å.

Table 3. Main characteristics of the different types of clay minerals

CLAST	**GARNIERITE**		
Mg-rich serpentine *(NC1, NC2)*	**Ni-rich serpentine** *NC1_green vein*	**Talc-like** *NC2_blue green vein* *NC3_green matrix*	**Sepiolite-like** *DR2_green matrix*
d_{001} = 7.3 Å (narrow peak; FWHM = 0.2 – 0.4°2θ) **d_{060} > 1.534 Å**	**d_{001} = 7.3 Å** (broad peak; FWHM = 0.9°2θ) **d_{060} < 1.534 Å**	**d_{001} = 10.2 Å** **d_{060} = 1.529 Å**	**d_{001} = 12.1 Å**

3.3. FTIR measurements

The spectra obtained by FTIR (spectral ranges of 3000-3800 cm^{-1} and 500-1200 cm^{-1}), are shown in figure 5. Each spectrum shows three series of absorption bands; the first between

3500 and 3750 cm^{-1}, the second between 800 and 1200 cm^{-1} and the third between 500 and 700 cm^{-1}.

The 3500-3700 cm^{-1} range is characteristic of the vibrations of hydroxyl groups associated with R-(O,OH) octahedra (where R = Mg or Ni) (Balan et al. 2002, Baron and Petit, 2016; Bishop et al. 2002). The 800-1200 cm^{-1} range corresponds to the stretching vibration modes of Si-O bonds (Balan et al. 2002). The 500-700 cm^{-1} range is assigned to bending vibration modes of OH groups bonds as well as Si-O and Si-O-R (where R = Mg or Ni) bonds (Balan et al. 2002; Bishop et al. 2002; Hofmeister and Bowey, 2006; Yariv and Heller-Kallai, 1975).

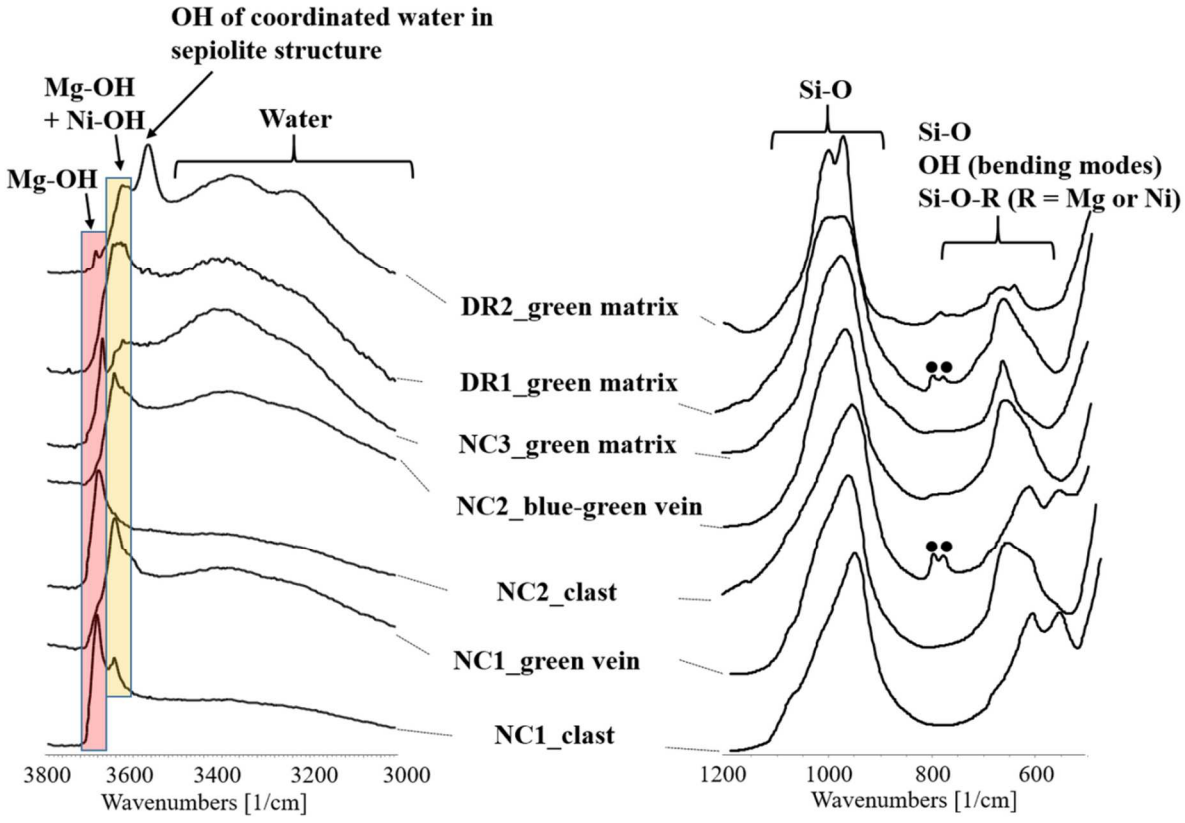

Figure 5. Infrared spectra of the selected samples, in the 3000-3800 cm^{-1} and 500-1200 cm^{-1} spectral ranges. Black circles correspond to quartz bands.

3.3.1. The 3500 – 3750 cm^{-1} region.

In this region there are one or more bands around 3600 cm^{-1}. However, since the absorption bands are relatively broad and complex, a second derivative treatment was performed for each spectrum in order to separate overlapping bands, and to determine the position of the main bands (Figure 6). The derivative has been calculated by a numerical method such as the one described by Savitzky and Golay (1964). This method is based on the derivative preceded by smoothing. Smoothing allows reducing the noise due to the derivative, which is amplified in the spectrum. In the present case, smoothing (using seven smoothing points) was applied using the Savizky-Golay algorithm.

The saprolite clasts from NC1 and NC2, mainly composed of Ni-poor serpentine, are characterized by a main band centered at 3687 cm^{-1} with a shoulder between 3694 cm^{-1} and 3698 cm^{-1}. Secondary bands with variable intensities are also visible around 3680 cm^{-1} and 3615 cm^{-1}. The positions of these bands are in accordance with observations by Baron and Petit (2016), and Jovanoski and Makreski (2016).

The garnierite composed of Ni-rich serpentine (NC1_green vein), differs from the Ni-poor serpentine from the saprolite by its main band at 3646 cm^{-1}. This band has shoulders at 3683 cm^{-1}, 3694 cm^{-1} and between 3600 cm^{-1} and 3620 cm^{-1}. These bands have similar positions as those observed in the saprolite clasts, but the intensity of the bands varies with the Ni content.

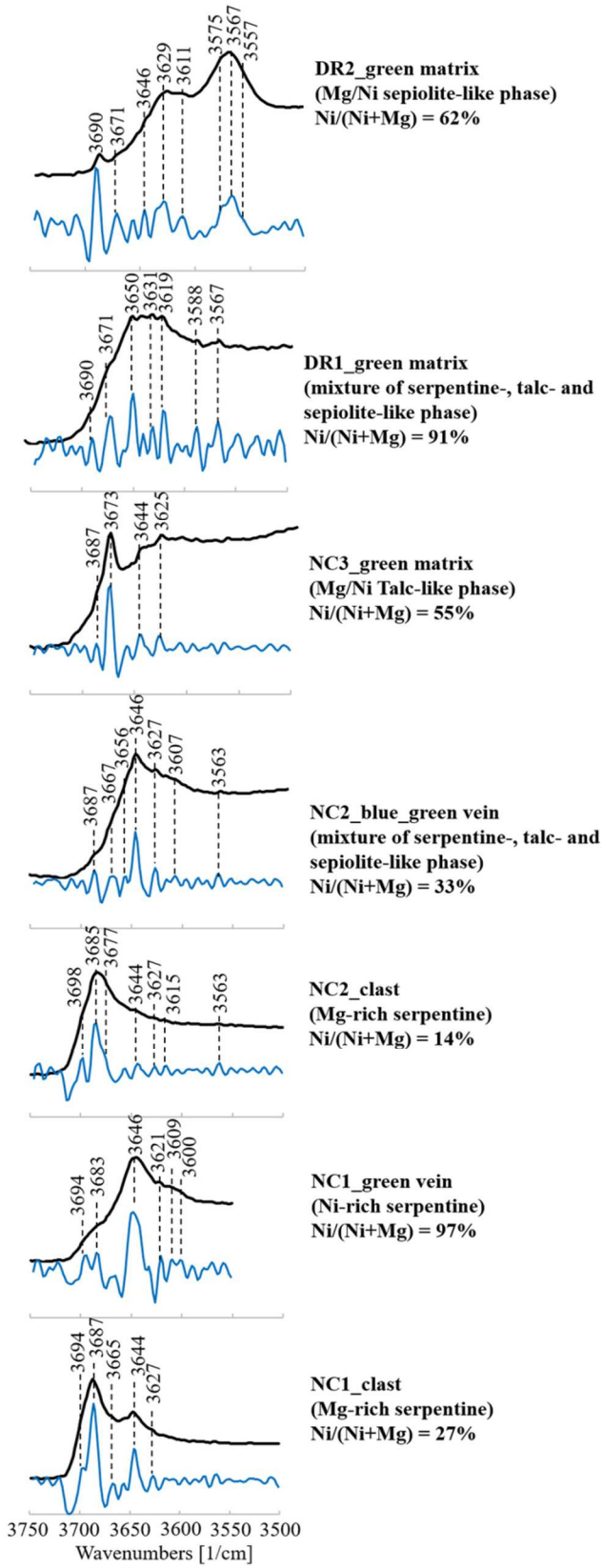

Figure 6. Infrared spectra of the selected samples in the 3500-3750 cm^{-1} region (black line) and their second derivative (blue line).

Regarding the talc-like ROI in the NC3 green matrix sample, the results are different from those of ROIs mainly composed of serpentine. In the present case, the main band is at 3675 cm^{-1}. This band is accompanied by other bands located at 3658 cm^{-1}, 3644 cm^{-1} and 3627 cm^{-1}. Interestingly, this spectrum has a relatively high baseline between 3660 cm^{-1} and 3500 cm^{-1}. This effect is due to the presence of water molecules absorbed onto the surfaces of the layers of the talc-like structure (Figure 5) (Brindley et al. 1979).

For the sepiolite-like ROI, in the DR2_green sample, the spectrum differs from those obtained in garnierite composed of serpentine-like or talc-like phases. There is a main band centered at 3567 cm^{-1}, accompanied by bands around 3690 cm^{-1} and 3631 cm^{-1}. The second derivative also reveals numerous bands located at positions equivalent to those detected in serpentine-like and talc-like ROIs (for example, the bands at 3671 cm^{-1} and 3646 cm^{-1}). However, XRD analyses only identified sepiolite-like phase. These results suggest that there are crystallographic similarities around the hydroxyl groups between these minerals.

For the samples with a more complex mineralogy, such as NC2_blue-green vein and DR1_green matrix, poorly or not well-resolved absorption bands characterize the spectra in the 3500-3750 cm^{-1} range. However, some positions of the main detected bands in the second derivative, can be assigned to serpentine-, talc- and sepiolite-like minerals, comparing with the previous spectra. Thus, for NC2_blue green vein ROI, the band at 3688 cm^{-1} reflects Ni-poor serpentine; the band at 3648 cm^{-1} can be ascribed to both Ni-rich serpentine and a talc-like phase, the band at 3629 cm^{-1} can be assigned to both talc-like and sepiolite-like phases. The last band at 3565 cm^{-1} can be attributed to a sepiolite-like phase. For the DR1_green matrix ROI, the presence of a talc-like phase is characterized by the band located at 3675 cm^{-1}. The band at 3652 cm^{-1} can be attributed to Ni-rich serpentine while the bands located at 3569 cm^{-1}, 3633 cm^{-1} and 3690 cm^{-1} correspond to sepiolite-like phases.

411 3.3.2. The 800 – 1200 cm^{-1} region.

412 In this region (Figure 7), except for the sepiolite-like ROI (DR2_green matrix), all the ROIs
413 are characterized by a broad and asymmetric band with a maximum located around 950-975
414 cm^{-1}, and shoulders between 1000 and 1100 cm^{-1}. These bands are characteristic of the
415 stretching vibrations of SiO_4 groups present in the structure of serpentine, talc and sepiolite
416 (Balan et al. 2002; Frost et al. 2001; Hofmeister and Bowey, 2006).

417 Comparison of the characteristic spectra of serpentine-like ROIs (in NC1 clast, NC1_green
418 vein and NC2 clast) shows that the band around 1010-1020 cm^{-1} is more pronounced in the
419 Ni-rich ROI (NC1_green vein) than in the Ni-poor ROI (NC2_clast). A slight shift of the
420 main band from 953 cm^{-1} for Ni-rich to 949 cm^{-1} for Ni-poor ROI is observed.

421 The talc-like phase spectrum, as shown in the NC3_green matrix ROI, has a wide band. It is
422 more symmetrical than that of serpentine. However, the second derivative reveals that the
423 positions are similar. Only variations in intensities are observed.

424 The sepiolite-like spectrum differs from that of serpentine- and talc-like ROIs by two well-
425 defined bands centered at 1005 cm^{-1} and 974 cm^{-1}. These bands have similar intensities.

426 For samples consisting of mixed phases (NC2_blue-green vein and DR1_green matrix), the
427 bands are more or less symmetrical. The intensity of the different bands, detected from the
428 second derivatives, is variable and probably related to the proportion of each phase within the
429 samples.

430

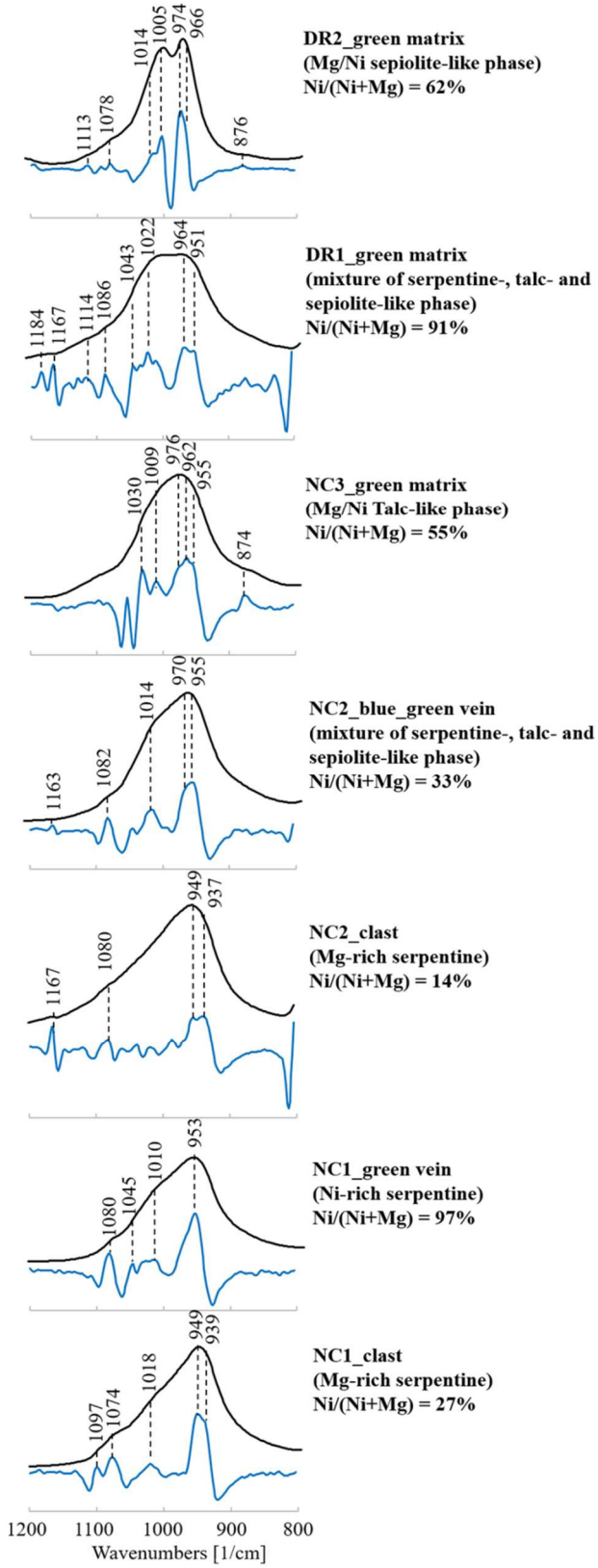

Figure 7. Infrared spectra of the selected samples in the 1200-800 cm^{-1} region (black line) and their second derivative (blue line).

435 3.3.3. The 500 – 700 cm^{-1} region.

436 The spectra obtained over this region, as well as their second derivatives, are shown in Figure
437 8. In general, the spectra are characterized by one or two main bands. For Ni-poor serpentine
438 from the saprolite clasts (NC1 and NC2_clasts), these bands are around 610 cm^{-1} and 554 cm^{-1}
439 ^{1}. The band at 610 cm^{-1} is wide and has shoulders towards high wavenumbers (625 cm^{-1}, 667
440 cm^{-1} and around 690 cm^{-1}).

441 In addition to band widening, the presence of Ni in serpentine-like phase causes a significant
442 difference in the intensity of the bands around 655-670 cm^{-1}, 610 cm^{-1} and 550-560 cm^{-1}. This
443 difference is visible in the spectrum of the NC1_green vein ROI, characteristic of a Ni-rich
444 serpentine. The band around 655-670 cm^{-1} becomes more intense with increasing Ni content.
445 In contrast, the band at 550-560 cm^{-1} tends to disappear.

446 The spectrum of the talc-like ROI (NC3_green matrix) is characterized by a main band
447 centered at 667 cm^{-1}. Remarkably, in contrast to serpentine-like phases, the bands around 610
448 cm^{-1} and 560 cm^{-1} are almost non-existent.

449 Unlike for serpentine- and talc-like phases, this region does not contain large and intense
450 bands in sepiolite-like phase (DR2_green matrix). The spectrum of sepiolite-like ROI differs
451 from the others by the absence of bands between 550 and 620 cm^{-1}, but is characterized by a
452 band centered at 644 cm^{-1}.

453

454

455

456

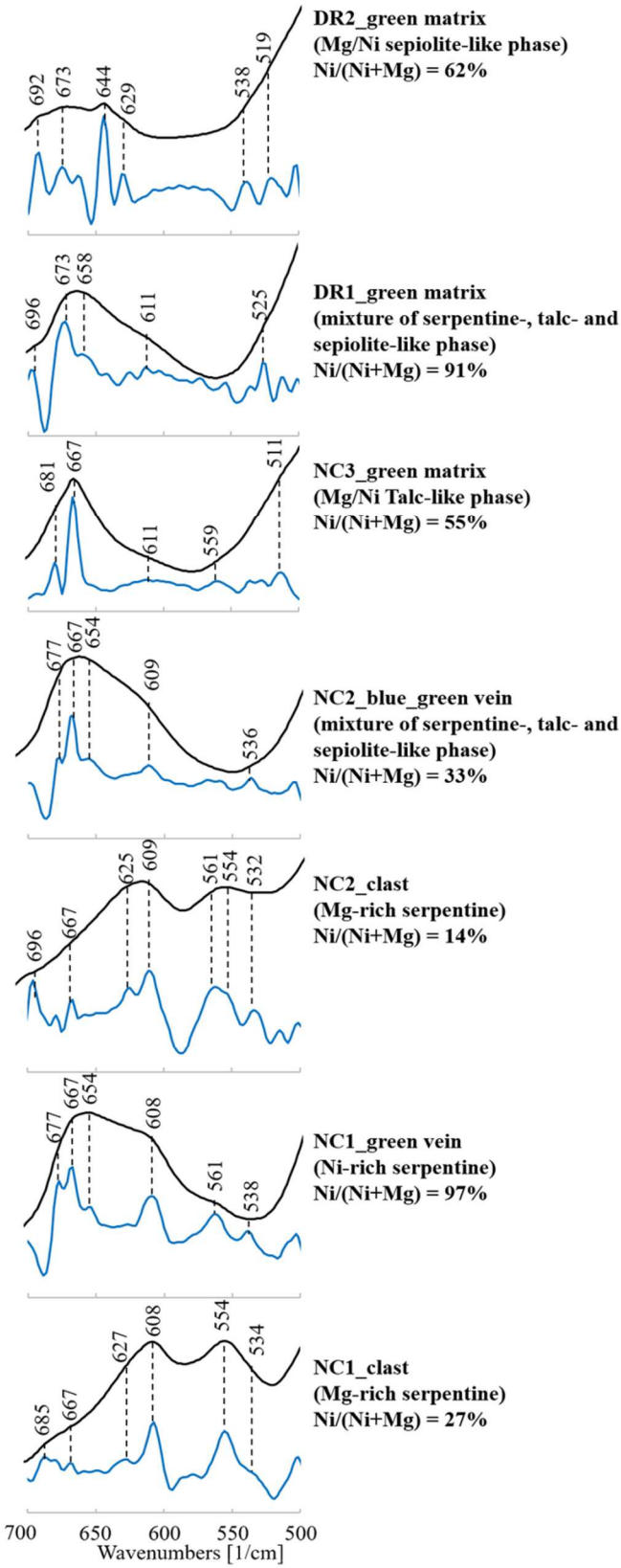

Figure 8. Infrared spectra of the selected samples in the 700-500 cm^{-1} region (black line) and their second derivative (blue line).

The spectra of ROIs consisting of a mixture of serpentine-like, talc-like and sepiolite-like phases (NC2_blue green vein and DR1_green matrix) show similar signatures. The spectra of NC2_blue green vein and DR1_green matrix have a larger band at 610 cm^{-1}, suggesting the presence of serpentine within the ROIs. In addition to that, the spectra show a contribution linked to a talc-like phase by a band at 667 cm^{-1} and 673 cm^{-1}, in NC2_blue-green vein and DR1 green matrix, respectively.

Table 4 presents a summary of the characteristic bands of the different types of minerals occurring in the studied samples. Each mineral group is characterized by distinct bands in the 3500 - 3700 cm^{-1} and 500-1000 cm^{-1} domains. In the serpentine spectra, the presence of Ni generates new bands, at 3646 cm^{-1} and 660 cm^{-1} which are not, or only slightly visible in Ni-poor serpentine. These bands can be used as indicators for the presence of Ni-rich serpentine. Concerning talc-like and sepiolite-like phases, the present data does not allow the identification of differences in the spectra that can be attributed to the Ni content.

Table 4. Summary of the main IR bands (in cm^{-1}) of the different types of phyllosilicates found in the studied ROIs.

CLAST	**GARNIERITE**		
Mg-rich serpentine *(NC1, NC2)*	**Ni-rich serpentine** *NC1_green vein*	**Talc-like** *NC2_blue green vein* *NC3_green matrix*	**Sepiolite-like** *DR2_green matrix*
3687	3646	3673	3690
		3625	3673
			3577
			3567
608	660	667	692
554	608	554	644

3.4. Raman spectroscopy

As well as FTIR analyses, Raman spectroscopy allows distinguishing the different phyllosilicates. The Raman spectra of the seven samples are shown in Figure 9. Each sample was analyzed over two regions. The first region, between 200 and 1200 cm^{-1}, corresponds to lattice and internal vibration modes, such as O-H-O vibrations and Si-O-Si vibrations (Auzende et al. 2004; Groppo et al. 2006). The second region, between 3500 and 3800 cm^{-1}, corresponds to the vibrations of the OH groups (e.g. Cathelineau et al. 2015, Villanova-de-Benavent et al. 2019).

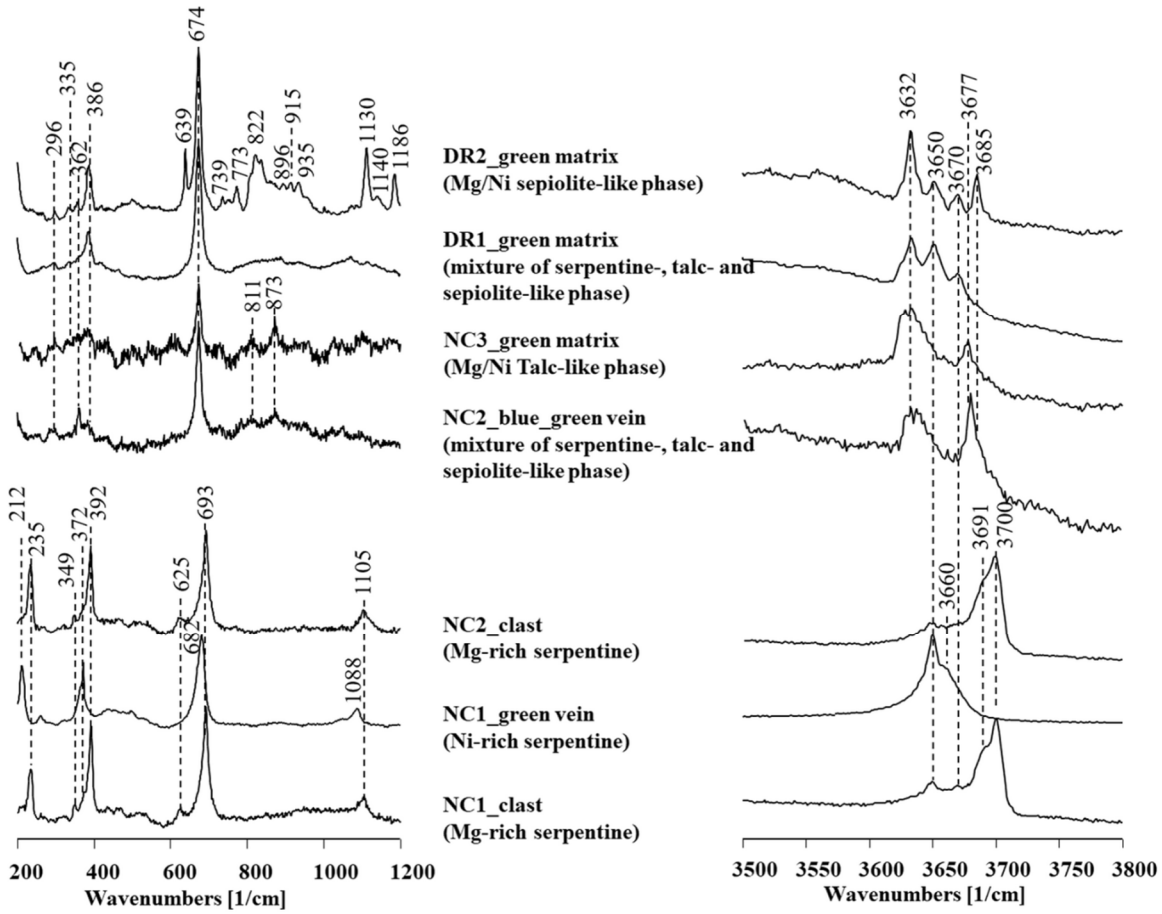

Figure 9. Raman spectra of the selected samples in the 200-1200 cm^{-1} and 3500-3800 cm^{-1} regions.

As the samples NC1 and NC2 present variations in the chemical composition at the micrometric scale (determined by EPMA), analyses were performed in different areas in order to study the influence of the Ni content on the Raman spectra of serpentine-like and talc-like phases. Analyses were carried out for Ni/(Ni+Mg) compositions ranging from 1 to 94% in the case of serpentine-like ROIs, and from 25 to 81% in the case of talc-like ROIs. The Raman spectra, linked to the corresponding chemical compositions are presented in Figure 10. The sepiolite-like ROI (DR2_green sample) has a more homogeneous Ni content, and therefore it was not considered for this part of the study.

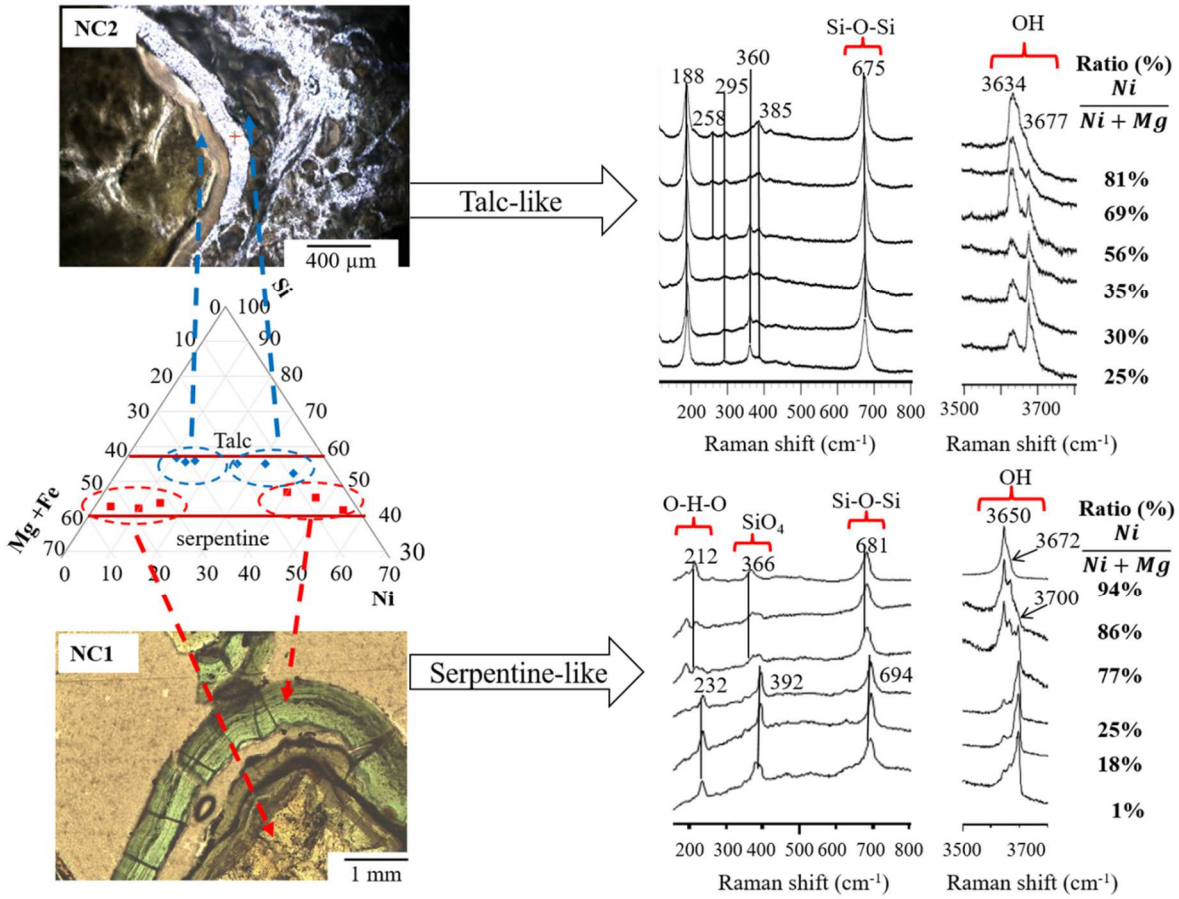

Figure 10. Optical photomicrographs (transmitted, parallel light) of the talc-like and the serpentine-like garnierites in samples NC2 and NC1, respectively, and their chemical composition, compared to their corresponding Raman spectra

3.4.1. The 200-1200 cm^{-1} region.

In this region Ni-poor serpentine (NC1 and NC2_clast, in figure 9) is characterized by five main bands located around 232 cm^{-1}, 392 cm^{-1}, 625 cm^{-1}, 694 cm^{-1} and 1105 cm^{-1}. Bands with similar positions are reported by Petriglieri et al. (2015) for lizardite and chrysotile. The band at 232 cm^{-1} is assigned to the O-H-O vibrations, the band at about 625 cm^{-1} to the OH-Mg-OH vibrations, while those at 392 cm^{-1}, 694 cm^{-1} and 1105 cm^{-1} involve the SiO_4 tetrahedral group (Auzende et al. 2004; Groppo et al. 2006; Petriglieri et al. 2015; Rinaudo et al. 2003).

The same bands are observed in Ni-rich serpentine (NC1_green vein), but with shifted positions towards shorter wavelengths. This shift as a function of the Ni content is also observed in Figure 10.

In the samples mainly composed of talc-like phases or mixtures of phases (NC2_blue green vein, NC3_green matrix and DR1_green matrix), the Raman spectra are characterized by two main bands located around 385 cm^{-1} and 675 cm^{-1}. Similar data were reported by Villanova-de-Benavent et al. (2019) for a garnierite composed mainly of kerolite-pimelite. Figure 10 shows that the Ni content has no influence on the band at 675 cm^{-1} in contrast to the band at 385 cm^{-1}. It turns out that when the mixture is Ni-poor, this same band is around 360 cm^{-1}. The Ni decrease in the mineral structure shifts progressively the intensity ratios between the bands at 360 and 385 cm^{-1} (I_{360} / I_{385}). By analogy with talc, these bands are located at 365 cm^{-1} and 675 cm^{-1} (Fumagalli et al. 2001; Wang et al. 2015) and are attributed to vibrations of Mg-OH bonds, and vibrations of Si-O-Si deformations, respectively (Fumagalli et al. 2001; Rosasco and Blaha, 1980). Also, it should be noted that the band located at 675 cm^{-1} varies in intensity from one analysis point to another (Figure 10). This variation may be due to the size and orientation of the grains analyzed (Sharma et al. 2000).

530 It is also noted that unlike talc, the samples from this study show a more or less wide and not
531 intense band between 800 and 900 cm^{-1}. This band may be related to vibrations of
532 deformation of Ni-OH bonds (Frost et al. 2008).
533 The DR2_green matrix ROI has a Raman signal that is relatively close to that of the previous
534 samples. It is characterized by the presence of bands at 386 cm^{-1}, 640 cm^{-1}, 675 cm^{-1}, between
535 750 and 850 cm^{-1} and above 1100 cm^{-1}. The main and only difference is the variable intensity
536 of some bands, depending on the talc-like or serpentine-like phases. Only McKeown et al.
537 (2002) indicate that peaks below 700 cm^{-1} involve the deformation vibrations of SiO_4
538 tetrahedra and $M(O,OH)_6$ octahedra, (where M=Mg, Ni), and those above 700 cm^{-1}, only of
539 SiO_4 tetrahedra.
540
541 3.4.2. The 3500-3800 cm^{-1} region.
542 As expected and in agreement with infrared spectroscopy, the region involving hydroxyl
543 groups shows many differences across the samples.
544 These differences are related both to the nature of the mineral phases analyzed (serpentine-,
545 talc- and sepiolite-like) and to the influence of the presence of Ni in the octahedral position.
546 This last point is particularly visible in figure 10, when comparing the Ni-poor serpentine or
547 talc with the Ni-rich ones. In the case of serpentine-like samples, Ni-poor serpentines are
548 characterized by a main band at 3700 cm^{-1} with a shoulder at 3690 cm^{-1}, and lower intensity
549 bands centered at 3650 cm^{-1} and 3665 cm^{-1}. Comparison of these positions with data from the
550 literature (Fritsch et al. 2016; Petriglieri et al. 2015; Tarling et al. 2018) on serpentine group
551 minerals (lizardite, chrysotile, antigorite) indicates that NC1 and NC2 clasts are most likely
552 composed of chrysotile.
553 The substitution of Mg by Ni in a serpentine-like structure results in relatively significant
554 changes. This goes through a broad and complex signal for a Ni/(Ni+Mg) ratio of 77% where

three main bands are found at 3650 cm^{-1}, 3672 cm^{-1} and 3700 cm^{-1}. These bands are attributed to the vibrations of the Ni_3-OH, (Ni,Mg)-OH and Mg_3-OH bonds, respectively (El Mendili et al. 2019). Then, the band at 3700 cm^{-1} disappears to give place to a main band centered at 3650 cm^{-1} with a shoulder around 3672 cm^{-1}, as observed in Ni-rich serpentine (NC1_green vein). In the present study, the effect of Ni caused a shift of the main band of about 50 cm^{-1}.

The Raman spectra of samples NC2 blue green vein and NC3 green matrix can be distinguished from serpentine-dominated samples by main bands centered at 3634 cm^{-1} and 3677 cm^{-1}. These bands have shoulders around 3640 cm^{-1} and 3686 cm^{-1}. Between these two main bands, the Raman spectrum of the NC3 green matrix ROI shows a band of low intensity centered at around 3660 cm^{-1}. All these results are consistent with those of Cathelineau et al. (2015) on Ni-Mg kerolite solid solutions.

In the sepiolite-like phase (sample DR2_green matrix), the Raman signal has four distinct bands. They are located at 3633 cm^{-1}, 3651 cm^{-1}, 3670 cm^{-1} and 3686 cm^{-1}. Their position is relatively close to those observed in more or less Ni-bearing individual serpentine-like and talc-like phase analyzed in this study.

Table 5 lists the main bands that differentiate between the analyzed Mg- and Ni-phyllosilicates. Each mineral group is distinguished by several characteristic bands, and within the same group (except sepiolite), Ni generates significant variations. All these differences make Raman spectroscopy a technique that can identify the presence of Ni in phyllosilicate ores.

Table 5. Main Raman bands (in cm^{-1}) of the different types of phyllosilicates in the studied ROIs

CLAST	**GARNIERITE**			
Mg-rich serpentine *(NC1, NC2)*	**Ni-rich serpentine** *NC1_green vein*	**Mg-rich talc-like** *NC2* *NC3_green matrix*	**Ni-rich talc-like** *NC2*	**Sepiolite-like** *DR2_green matrix*
3700	3650	3677	3634	3686 3670 3651 3633
694 392 232	681 366 212	675 360 295 188	675 385 295 258 188	> 1100 750-850 640 386

4. DISCUSSION

4.1. Influence of Ni on the shape and position of X-ray diffraction peaks

The X-ray diffractograms obtained in the present study are characterized by relatively broad peaks. This effect seems to be related to a difference of crystallinity caused by the presence of Ni within the structure of the minerals. It is particularly visible when comparing the serpentine-like phases encountered in samples NC1 and NC2 ROIs. The peaks, especially the main peak at 7.3 Å, broaden with the Ni content. This observation was also made by Brindley and Wan (1975) in their study of lizardite-népouite system, where broader peaks are due to small coherent domains and structural disorders caused by the presence of Ni in octahedral

595 sites. Similar broadening was observed at the 10.2 Å peak, characteristic of talc-like phases,
596 by Brindley et al. (1977, 1979), Cathelineau et al. (2015), Martin de Vidales et al. (1991) and
597 Villanova-de-Benavent et al. (2014).
598 The substitution of Mg by Ni in the octahedral position has also an effect on the position of
599 the (060) reflection. This is directly related to the crystallographic parameter *b*. In the present
600 study, this effect is visible in the diffractograms of serpentine-dominated samples, where the
601 (060) reflections are located at 1.537 Å, 1.534 Å and 1.530 Å for NC2_clast, NC1_clast and
602 NC1_green vein, respectively. As indicated by Baron and Petit (2016), the variation observed
603 for the (060) reflection is due to the atomic radii difference between Mg and Ni in the
604 octahedral coordination. In their study on the lizardite-népouite series ($(Mg_{3-x}Ni_x)Si_2O_5(OH)_4$),
605 these authors established a correlation between the position of the (060)
606 reflection and the Ni content. This can be written as follows: d_{060} (Å) = -0.0026x + 1.5374, for
607 x between 0 (lizardite) and 3 (népouite). From this relationship, it can be estimated that Ni in
608 the structural formula is of 0.15, 1.31 and 2.85 atoms per formula unit for NC2_clast,
609 NC1_clast and NC1_green vein, respectively. From the chemical analyses (EPMA), the
610 values of x are 0.17, 0.37 and 2.58 for the same samples. These results are reported in figure
611 11 and compared to the data by Baron and Petit (2016). Except for NC1_clast, the comparison
612 shows that the results are relatively close to the correlation proposed by Baron and Petit
613 (2016). It confirms that the position of the (060) reflection is an indicator of the presence of
614 Ni in serpentine-like phases. For sample NC1_clast, there is a deviation from the correlation.
615 However, due to lack of data, it is difficult to know if this deviation is related to the nature of
616 the sample (synthetic in Baron and Petit (2016) and natural in this study), or to the chemical
617 composition of the sample. In our case, the composition is based on point analyses and not on
618 the bulk sample. In addition, it is important to mention that amorphous compounds rich in Ni
619 can also be associated with garnierites (Cluzel and Vigier, 2008) and are not detected by

620 XRD. The chemical composition of the material may be influenced by this association and
621 generate a deviation between the position of the (060) reflection peak and the Ni content. In
622 the present case, more statistics are needed.

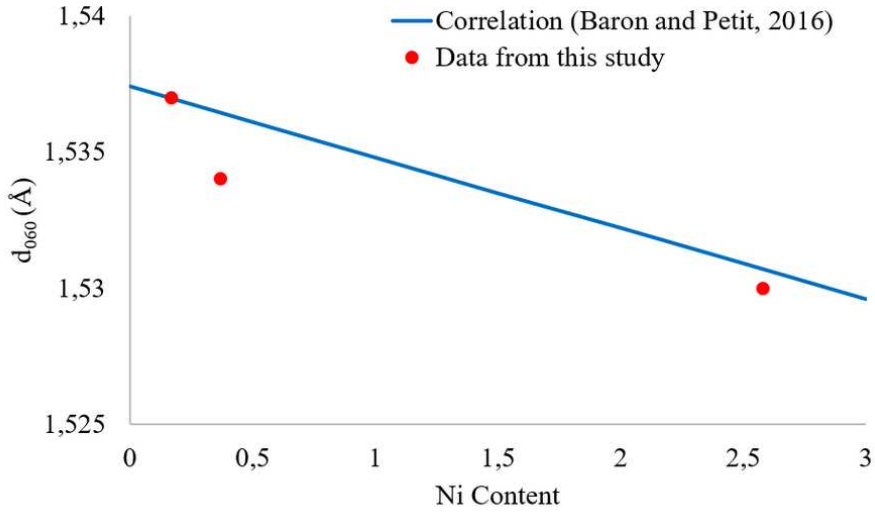

623

624 Figure 11. Comparison between d_{060} position and Ni content in serpentine-like samples.

625

626

627 Samples containing talc-like phases such as NC2_blue green vein, NC3_matrix and
628 DR1_matrix, display a (060) reflection with a position varying between 1.526 Å and 1.529 Å.
629 These positions are similar to those observed by Brindley et al. (1979) on five kerolite-
630 pimelite samples. The observed variations may be related to different Ni contents, but also to
631 the presence of serpentine-like phases in the NC2 and DR1 samples.
632 For sepiolite-like phases, substitution of Mg by Ni forms a series of solid solutions between
633 Mg end-member, sepiolite and Ni-end member, falcondoite. Tauler et al. (2009) showed that
634 there are little differences among diffractograms of various sepiolite-falcondoite solid-
635 solutions. From a structural point of view, they mainly noted an influence on the cell
636 parameter *a,* which tends to decrease with the Ni content. In this study, there is not sufficient
637 data to confirm this statement.

638

639 4.2. FTIR – influence of Ni on the position of the characteristic bands

640

641 4.2.1. Ni effect on the hydroxyl groups bands

642 The characteristic bands of the stretching and bending vibration modes of the hydroxyl groups
643 are located in the 3500-3750 cm^{-1} and 500-700 cm^{-1} ranges, respectively (Balan et al. 2002;
644 Baron and Petit, 2016; Brindley et al. 1979; Frost et al. 2001; Yeniyol, 2014). As the hydroxyl
645 groups are linked to cations in octahedral positions, the position of these bands is influenced
646 by the substitution of Mg by Ni.

647 For serpentine-like phases, this substitution generates a significant difference in the position
648 of the main bands. They are at 3685 cm^{-1}, 610 cm^{-1} and 554 cm^{-1} in Ni-poor serpentine (NC2
649 clast) and at 3646 cm^{-1}, 667 cm^{-1} and 608 cm^{-1} in Ni-rich serpentine (NC1_green vein). Baron
650 and Petit (2016) obtained similar results in the lizardite-népouite series. They assigned the
651 band at 3685 cm^{-1} to the stretching vibrations of Mg-OH. The band at 3646 cm^{-1} corresponds
652 to the stretching vibrations of Ni-OH. In the present study, these two bands were detected in
653 the three samples that are mainly composed of serpentine-like phases. However, they display
654 different intensities. Baron and Petit (2016) observed that the intensity of the band at 3646
655 cm^{-1} increases progressively with the Ni content, while the intensity of the band at 3687 cm^{-1}
656 decreases. This finding is particularly important as it shows that the intensity of the 3646 cm^{-1}
657 band is indicative for the presence of Ni. The intensity of this band is low in NC2_clast and
658 significant in NC1_green vein. Based on the chemical composition, coherent with the
659 estimation of Ni content by XRD, the NC1_clast has an intermediate composition between
660 Ni-poor (NC2_clast) and Ni-rich serpentine-like phases (NC1_green vein). In particular, this
661 sample shows that both bands (3687 cm^{-1} and 3646 cm^{-1}) are relatively well defined. As

662 expected, the intensity of the band at 3646 cm^{-1} is higher than in NC2_clast but lower as in the
663 NC1_green vein.
664 In the 500-700 cm^{-1} region, the band around 655-670 cm^{-1} is characteristic of Ni-(O,OH) bond
665 vibrations in Ni-rich serpentines (Baron and Petit, 2016; Brindley et al. 1979). The equivalent
666 (Mg-(O,OH)) bond appears at 550-560 cm^{-1} for Ni-poor serpentine. Our results are in
667 agreement with these assignments, since they highlight that the 550-560 cm^{-1} band tends to
668 disappear, while the band at 655-670 cm^{-1} increases with Ni content (NC1_green vein).
669 For talc-like phases, four bands are reported in the 3500-3750 cm^{-1} region, at 3687 cm^{-1}, 3675
670 cm^{-1} (main band), 3644 cm^{-1} and 3625 cm^{-1}. These positions are in accordance with published
671 data (Gerard and Herbillon (1983), Hofmeister and Bowey (2006), Jovanoski and Makreski
672 (2016)). They correspond to four different environments of hydroxyl groups (variable
673 distances of the R-OH groups, with R = cation in octahedral position) within the talc structure
674 (Gerard and Herbillon, 1983). According to these authors, the substitution of Mg by Ni
675 influences the intensity of these bands, particularly those located at 3675 cm^{-1} and 3625 cm^{-1}.
676 The intensity of the band at 3675 cm^{-1} decreases as the Ni content increases. The opposite
677 phenomenon occurs for the band at 3627 cm^{-1}. This is similar to the effect observed in the
678 serpentine-like phase with the bands at 3687 cm^{-1} and 3646 cm^{-1}. The observation by Gerard
679 and Herbillon (1973) suggests that the intensity of the band located at 3625 cm^{-1} may be an
680 indicator of the presence of Ni in a sample with high amounts of talc-like phases.
681 In the 500-700 cm^{-1} region, the band at 667 cm^{-1} is well resolved and corresponds to both the
682 Mg-OH bending vibrations and the Si-O bond vibrations present in the Mg-rich talc-like
683 phase (Gerard and Herbillon, 1973; Brindley et al., 1979). According to Wilkins and Ito
684 (1967), the equivalent band occurs in higher frequencies (670-690 cm^{-1}) in Ni-rich talc. This
685 suggestion allows us to propose that the band detected at 681 cm^{-1} in the NC3_green matrix
686 sample can be attributed to the presence of Ni.

687 For the sepiolite-like phase (DR2_green matrix), the main bands which involve the vibration
688 of hydroxyl groups, are at 644 cm^{-1}, 3567 cm^{-1}, 3629 cm^{-1} and 3690 cm^{-1}. These data are
689 consistent with those of Frost et al. (2001) from sepiolite of various origins. They observed
690 band positions around 649 cm^{-1}, 3565 cm^{-1}, 3620 cm^{-1} and 3690 cm^{-1}, in addition to bands
691 centered at around 3430 cm^{-1} and 3230 cm^{-1}, which are attributed to the vibrations of the
692 water molecules (the two latter bands are not shown in the present study). In the case of
693 falcondoite, Chukanov (2014) reports three bands centered at 3677 cm^{-1}, 3628 cm^{-1} and 3575
694 cm^{-1}. Our findings show that the second derivative of the spectrum reveals similar bands at
695 3673 cm^{-1}, 3631 cm^{-1} and 3577 cm^{-1}. On the base of the comparison with the literature, we
696 propose the bands located at 3673 cm^{-1} and 3577 cm^{-1} to be characteristic for the presence of
697 nickel within the structure (vibrations of the Ni-OH bonds) while the bands at 3567 cm^{-1} and
698 3690 cm^{-1} are characteristic of the presence of Mg (vibrations of the Mg-OH bonds). The
699 3629 cm^{-1} band can be attributed to both Mg and Ni, in the case of an intermediate
700 composition within sepiolite-falcondoite solid-solution, as in our study.
701
702 4.2.2. Nickel effect on silicate bands (FTIR)
703 For the seven samples, the same absorption bands are generally found around 950-960 cm^{-1},
704 1000-1030 cm^{-1} or around 1090 cm^{-1}. All samples have vibration bands of the Si-O bonds of
705 serpentine, talc and sepiolite, making the mineral identification difficult (Figs. 12 A, B and
706 C). This observation is supported by data from the literature, all displayed in figure 12.
707 Although our study indicates an effect of the presence of Ni on the intensity of the band
708 around 1010 cm^{-1}, literature data show that for the same type of phase, there is no relationship
709 between the bands observed and the substitution of Mg by Ni.

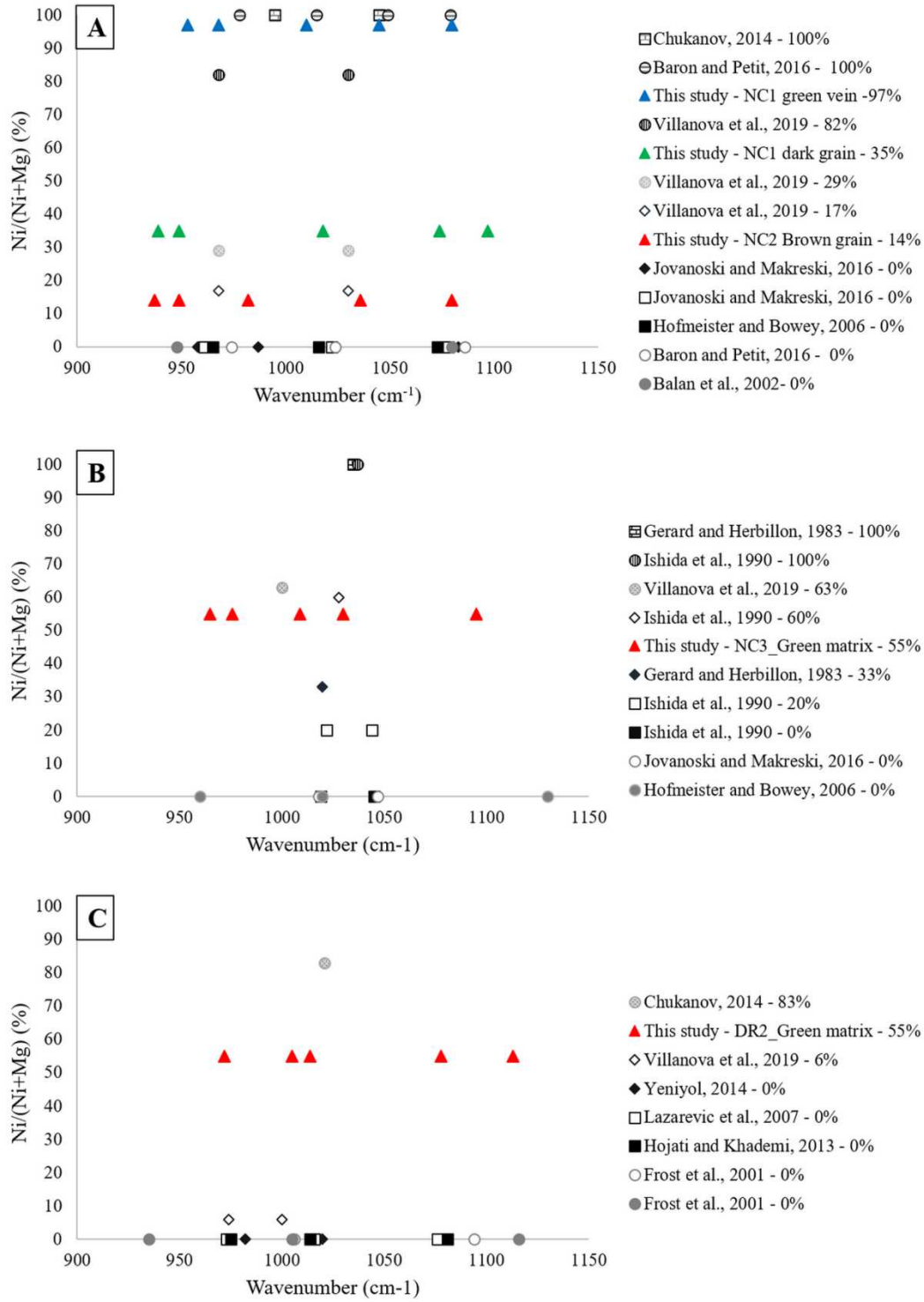

710

711 Figure 12. Positions of the vibration bands in the 900-1150 cm^{-1} range observed in this study,
712 compared with those from the literature, for serpentine-like phases (A), talc-like phases (B)
713 and sepiolite-like phases (C). The percentage indicated next to the authors corresponds to the
714 Ni/(Ni+Mg) ratio calculated from the chemical composition or the structural formulae
715 mentioned in the published articles.

These variations can have several origins. It may be due to the nature of the mineral within the same mineral group, such as lizardite, chrysotile, antigorite (serpentine group), and/or, its origin (natural/synthetic, various formation conditions). Moreover, as in our study, quartz is also detected (NC2_clast) having absorption bands between 900 and 1100 cm^{-1} (Liang et al. 2006).

An important point to mention is the influence of data processing on the higher precision on band number and positions obtained. Indeed, some studies mention only the maximum intensities observed (Balan et al. 2002; Gerard and Herbillon, 1983; Ishida, 1990), while others have carried out deconvolution or mathematical treatments such as second derivatives (Frost et al. 2001; Baron and Petit, 2016; Jovanosky and Makreski, 2016). Our study clearly shows that mathematical data treatments bring higher resolution on a spectral area giving information that is more precise.

4.3. Raman spectroscopy – influence of nickel on the position of the characteristic bands

The substitution of Mg by Ni generates shifts on most bands. These shifts can be important, especially for those involving hydroxyl groups (mainly in the 3500-3800 cm^{-1} range), but also for those characterizing the vibrations of SiO_4 groups. This is observed in the case of serpentine with a shift towards lower wavenumbers of about 15 to 20 cm^{-1}.

This shift can be attributed to the Ni-enrichment mechanisms of serpentine in the NC1 sample (Majumdar et al. 2014; Putnis, 2009). Such shifts are reported for various mineral replacements (Hövelmann et al. 2010; Niedermeir et al. 2009; Putnis et al. 2007) and may be associated with dissolution-precipitation mechanisms (Putnis, 2009). One consequence is probably the modification of the environment of SiO_4 tetrahedra (Wang et al. 2015). According to Hooke's law equation, which relates the wavenumber υ to the force constant k, according to the following equation $\upsilon = \frac{1}{2\pi}\sqrt{\frac{k}{\mu}}$, which relates the wavenumber υ to the force

741 constant k, and where μ is the reduced mass, the weaker the force constant, the lower the
742 wavenumber. In the present case, the fact that the Raman bands of the Ni-rich serpentine
743 decrease indicates weaker Si-O bonds. However, in our study, the observed shift only
744 concerns the Ni-rich serpentine from sample NC1. Depending on the origin and the
745 mechanisms involving the formation of the Ni-rich serpentine, the shift may not be observed.
746 This may also be one of the reasons why no correlations are observed from the FTIR data on
747 the characteristic bands of SiO_4 (Figure 12).
748 For bands involving hydroxyl groups, the nature of the cation in the octahedral position
749 (Mg^{2+}, Ni^{2+}) generates a relatively large shift, which can reach 50 cm^{-1}. Because of a
750 difference in bond lengths (Ni-OH is longer than Mg-OH), the metal–hydroxyl bond has a
751 lower force constant when Ni is present.
752 In addition to band shifts, we noted variations in intensity ratios between several bands, which
753 tends to correlate with the Ni content. This is particularly the case for talc-like phases,
754 between the bands at 360 cm^{-1} and 385 cm^{-1} (I_{360}/I_{385}) and between 3636 cm^{-1} and 3677 cm^{-1}
755 (I_{3634}/I_{3677}) (Figure 9), in agreement with those reported by Cathelineau et al. (2015). They
756 showed that the bands located between 3620 and 3660 cm^{-1} tend to increase with the Ni
757 content, while those above 3675 cm^{-1} tend to decrease. In our study, the intensity ratio of the
758 two main bands (I_{3634} / I_{3677}) is higher with a higher Ni content.
759 For sepiolite, the Raman spectra obtained do not allow determining a possible influence of
760 nickel. There is no precise attribution for each band and there are few or no Raman spectra of
761 sepiolite or falcondoite in literature (Frost et al. 2001; Villanova-de-Benavent et al. 2019). It
762 can only be noted that the characteristic bands of this series are relatively close to those
763 observed in serpentines and talc-like phases. This can be explained by similar environments
764 around Mg^{2+} and Ni^{2+} cations although their crystallographic structure is different.
765

5. Implications for Ni-laterite deposit mineral library databases used for in-field analyses

In recent years, more and more projects are concerned with developing expert systems combining mineralogical, chemical and textural analyses (Duée et al. 2019; El Mendili et al. 2019). In the case of Ni mining exploration, studies focus on the characterization of various garnierites in order to determine indicators of the presence of Ni-bearing phases. Figure 13 is a summary of the main results obtained in this study. It highlights the characteristic signs of each compound analyzed and shows the value of combining several analytical techniques to identify the mineralogy and phases of interest. Indeed, in the present case, this study showed that XRD allows to easily differentiate clay mineral families by the 001 peak, but this technique is limited to give an indication of the presence of Ni within the samples. Conversely, vibrational spectroscopies show similar characteristics from one clay mineral family to another, by the presence of more or less large bands on domains of similar wave numbers. However, these techniques have a sensitivity on the substitutions which can take place within a mineral by shifts of the characteristic bands of the M-OH bonds, with M = Mg or Ni. The combination of these techniques, summarized in Figure 13, therefore offers the advantage of unambiguous mineral identification. The serpentine-like phases are characterized by a basal distance d_{001} located around 7.3 Å and the presence of Ni evidenced by the presence of FTIR and Raman bands centered around 3650 cm^{-1}. Talc-like phases are characterized by XRD with a peak around 10.2 Å. The presence of Ni is detected by FTIR and Raman bands centered respectively around 3625 cm^{-1} and 3634 cm^{-1}. In the presence of Mg, these bands are shifted at around 3670 cm^{-1}. Finally, sepiolite-like phases are distinguished by a basal distance of about 12.1 Å. Data obtained by FTIR suggest that the presence of Ni can be detected by bands around 3673 cm^{-1} and 3577 cm^{-1}. However, for this

type of compounds, further investigations are needed to provide further signals characteristic of the presence of Ni.

The development of on-line mineralogical and chemical analysis systems, with existing databases such as the Crystallography Open Database (COD), and the Raman Open Database (ROD) integrating these results, is a real opportunity to identify on site and in near real time the areas of interest for mineral exploration.

Serpentine-like Mg	Serpentine-like Ni	Talc-like Mg	Talc-like Ni	Sepiolite-like Mg	Sepiolite-like Ni
XRD					
d_{001} = 7.3 Å d_{060} = 1.537 Å	d_{001} = 7.3 Å d_{060} = 1.530 Å	d_{001} = 10.2 Å	d_{001} = 10.2 Å	d_{001} = 12.1 Å	d_{001} = 12.1 Å
IR (main bands in cm^{-1})					
3687 950-960 608 554	3646 950-960 660 608	3673 960-980 667 554	3625 960-980 667 554	3690 3567 1005 972 644	3673 3577 1005 972 644
Raman (main bands in cm^{-1})					
3700 694 392 232	3650 681 366 212	3677 675 360 295 188	3634 675 385 295 258 188	3686 3670 3651 3633	

Figure 13. Main characteristics of the different minerals analyzed in this study.

6. Conclusions

This study focused on the characterization of garnierite facies of different colors, mineralogy, chemical composition and spectral features. Our data can feed open databases which are useful for in-field analyses during exploration and mining of Ni-laterites. The characteristic signals allow: 1) the identification of Ni-rich phases and their nature (serpentine, talc and sepiolite) and 2) an estimation of the Ni content. These data find particular application using

806 the XRD-XRF benchtop systems (e.g. Equinox, Thermofisher), which are used on mine sites
807 or processing plants.
808 This study on Ni-rich and Ni-poor phyllosilicates from garnierite and the host saprolite shows
809 that the presence of Ni has a significant impact on the crystallographic structure and
810 crystallinity of phyllosilicates. It can be observed in the XRD diffractograms and FTIR and
811 Raman spectra. From an XRD point of view, this results in a widening of the main peaks and
812 a shift of the d_{060} reflection, visible in the serpentine. From a vibrational spectroscopic point
813 of view, the substitution of Mg by Ni generates shifts in the characteristic bands of the bonds
814 involving the relatively large OH groups (of the order of 50 cm^{-1}). Moreover, Raman analyses
815 also showed that as a function of the Ni and Mg content, the intensity ratio of Mg-OH/Ni-OH
816 bands decreases progressively with the Ni content, in serpentine-like as well as talc-like
817 phases.
818 Finally, this study shows the importance of combining the different analytical techniques to
819 unambiguously interpreting the data. In the case of Ni laterite exploration, the combined use
820 of these techniques connected to databases including detailed information on Ni mineralogy
821 offers encouraging prospects for improving and facilitating in-field analysis.
822 Finally, smart mathematical data treatment allows higher resolution of single spectral regions.
823
824
825 **Acknowledgement**
826 This study was performed in the frame of the SOLSA project (EU H2020 G.A. No. 689868.).
827 The authors thank Eramet-SLN for providing a garnierite sample. M. Alleki is also thanked
828 for sample preparation. Thanks to the two reviewers, the paper could be improved.
829
830 **References**
831 Anawati J., Yuan R., Kim J., Azimi G. (2020) Selective Recovery of Scandium from
832 Nickel Laterite Ore by Acid Roasting–Water Leaching. In: Azimi G., Forsberg K.,

833 Ouchi T., Kim H., Alam S., Baba A. (eds) Rare Metal Technology 2020. The
834 Minerals, Metals & Materials Series. Springer, Cham. https://doi.org/10.1007/978-3-
835 030-36758-9_8.
836
837 Auzende, A.L., Daniel, I., Reynard, B., Lemaire, C., Guyot, F. (2004). High-pressure
838 behavior of serpentine minerals: a Raman spectroscopic study. Physics and Chemistry
839 Minerals, 31, 269-277
840 Balan, E., Saitta, A.M., Mauri, F., Lemaire, C., Guyot, F. (2002) First-principles calculation
841 of the infrared spectrum of lizardite. American Mineralogist, 87, 1286-1290
842 Baron, F., Petit, S. (2016) Interpretation of the infrared spectra of the lizardite-nepouite series
843 in the near- and mid-infrared range. American Mineralogist, 101, 423-430
844 Berger, V.I., Singer, D.A., Bliss, J.D., and Moring, B.C., (2011) Ni-Co laterite deposits of the
845 world; database and grade and tonnage models: U.S. Geological Survey Open-File Report
846 2011-1058 [*http://pubs.usgs.gov/of/2011/1058/*]
847 Bish, D.L., Brindley, G.W. (1977) A reinvestigation of takovite, a nickel aluminium hydroxy-
848 carbonate of the pyroaurite group. American Mineralogist, 62, 458-464
849 Bishop, J., Murad, E., Dyar, M.D. (2002) The influence of octahedral and tetrahedral cation
850 substitution on the structure of smectites and serpentines as observed through infrared
851 spectroscopy. Clay Minerals, 37, 617-628
852 Bosio, N.J., Hurst, V.J., and Smith, R.L. (1975) Nickeliferous nontronite, a 15 A ˚ garnierite,
853 at Niquelândia, Goia´s, Brazil. Clays and Clay Minerals, 23, 400-403
854 Brindley, G.W. (1980) The structure and chemistry of hydrous nickel-containing silicate and
855 nickel-aluminium hydroxyl minerals. Bulletin de Minéralogie, 103, 161-169
856 Brindley, G.W., Hang P.H.M. (1973) The nature of garnierites – I. Structures, chemical
857 compositions and color characteristics. Clays and Clay Minerals, 21, 27-40

858 Brindley, G.W., Wan H.M. (1975) Compositions, structures and thermal behavior of nickel-
859 containing minerals in the lizardite-nepouite series. American Mineralogist, 60, 863-871
860 Brindley, G.W., Bish, D.L., Wan H.M. (1977) The nature of kerolite, its relation to talc and
861 stevensite. Mineralogical Magazine, 41, 443-452
862 Brindley, G.W., Bish, D.L., Wan H.M. (1979) Compositions, structures, and properties of
863 nickel-containing minerals in the kerolite-pimelite series. American Mineralogist, 64, 615-
864 625
865 Bruker. (2017) TOPAS V6.0. Bruker AXS, Karlsruhe, Germany
866 Butt, C. R., and Cluzel, D. (2013). Nickel laterite ore deposits: weathered serpentinites.
867 Elements, 9(2), 123-128.
868 Cathelineau, M., Caumon, M.C., Massei, F., Brie, D., Harlaux, M. (2015) Raman spectra of
869 Ni-Mg kerolite: effect of Ni-Mg substitution on O-H stretching vibrations. Journal of
870 Raman Spectroscopy, 46, 933-940
871
872 Cathelineau, M., Quesnel, B., Gautier, P., Boulvais, P., Couteau, C., Drouillet, M. (2016)
873 Nickel dispersion and enrichment at the bottom of the regolith: formation of pimelite
874 target-like ores in rock block joints (Koniambo Ni deposit, New Caledonia). Mineralogical
875 Deposita, 51, 271-282
876 Chassé, M., Griffin, W. L., O'Reilly, S. Y., and Calas, G. (2016). Scandium speciation in a
877 worldclass lateritic deposit. Geochemical Perspectives Letter 3, 105–114.
878 Chassé, M., Griffin, W. L., O'Reilly, S. Y., and Calas, G. 2019. Australian laterites reveal
879 mechanisms governing scandium dynamics in the critical zone. Geochimica et
880 Cosmochimica Acta, 260, 292-310.
881 Chukanov, N.V. (2014). Infrared spectra of minerals species : Extended library. Springer
882 Geochemistry/Mineralogy. Springer Science+Business Media, Dordrecht (The
883 Netherlands). pp.1726

884 Cluzel, D., Vigier, B. (2008). Syntectonic mobility of supergene nickel ores of New
885 Caledonia (Southwest Pacific). Evidence from garnierite veins and faulted regolith.
886 Resource Geology, 58, 161-170
887 Dalvi A.D., Bacon, W.G., Osborne, R.C. (2004).The past and the future of nickel lateirtes. In
888 PDAC 2004 International Conference Trade Show and investors exchange, Toronto,
889 Canada, March 7-10, Proceedings Toronto, Canada, Prospectors and Developers
890 Associations of Canada, 27p.
891 Decarreau, A., Colin, F., Herbillon, A., Manceau, A., Nahon, D., Paquet, H., Trauth-Badaud,
892 Trescases (1987). Domain Segregation in the Ni-Fe-Mg smectites. Clays and Clay
893 Minerals, V. 35, 1, 1-10
894 Duée, C., Orberger, B., Maubec, N., Laperche, V., Capar, L., Bourguignon, A., Bourrat, X.,
895 El Mendili, Y., Chateigner, D., Gascoin, S., Le Guen, M., Rodriguez, C., Trotet, F., Kadar,
896 M., Devaux, K., Ollier, M., Pillière, H., Lefèvre, T., Harang, D., Eijlkelkamp, F., Nolte, H.,
897 Koert, P. (2019). Impact of heterogeneities and surface roughness on pXRF, pIR, XRD and
898 Raman analyses: Challenges for on-line, real-time combined mineralogical and chemical
899 analyses on drill cores and implications for “high speed” Ni-laterite exploration. Journal of
900 Geochemical Exploration, 198, 1-17
901 El Mendili, Y., Chateigner, D., Orberger, B., Gascoin, S., Bardeau, J.F., Petit, S., Duée, C., Le
902 Guen, M., Pillière, H. (2019). Combined XRF, XRD, SEM-EDS, and Raman analysis on
903 serpentinized harzburgite (nickel laterite mine, New Caledonia): implications for
904 explorations and geometallurgy. ACS Earth and Space Chemistry, 3,10, 2237-2249
905 El Mendili, Y., Orberger, B., Chateigner, D., Bardeau, J.F., Gascoin, S., Petit, S., Khadraoui,
906 F. (2020). Insight into the structural, elastic and electronic properties of a new
907 orthorhombic 6O-SiC polytype. SCIENTIFIC REPORTS | (2020) 10:7562 |
908 HTTPS://DOI.ORG/10.1038/S41598-020-64415-4

909 Freyssinet P, Butt CRM, Morris RC, Piantone P (2005) Ore-forming processes related to
910 lateritic weathering. In: Hedenquist JW, Thomson JFH, Goldfarb RJ, Richards JP (eds),
911 Economic Geology100th Anniversary Volume. Economic Geology Publishing Company,
912 New Haven, Connecticut, pp 681-722
913 Fritsch, E., Juillot, F., Dublet, G., Fonteneau, L., Fandeur, D., Martin, E., Caner, L., Auzende,
914 A.L., Grauby, L., Beaufort, D. (2016). An alternative model for the formation of hydrous
915 Mg/Ni layer silicates ('deweylite'/'garnierite') in faulted peridotites of New Caledonia: I.
916 Texture and mineralogy of a paragenetic succession of silicate infillings. European Journal
917 of Mineralogy, 28, 295-311
918 Frost, R.L., Jagannadha Reddy, B., Dickfos, M.J. (2008). Raman spectroscopy of the nickel
919 silicate mineral pecoraite – an analogue of chrysotile (asbestos). Journal of Raman
920 Spectroscopy, 39, 909-913
921 Frost, R.L., Locos, O.B., Ruan, H., Kloprogge, J.T. (2001). Near-infrared and mid-infrared
922 spectroscopic study of sepiolites and palygorskites. Vibrational Spectroscopy, 27, 1-13
923 Fumagalli, P., Stixrude, L., Poli, S., Snyder, D. (2001). The 10Å phase: a high-pressure
924 expandable sheet silicate stable during subduction of hydrated lithosphere. Earth and
925 Planetary Science Letters, 186, 125-141.
926 Gerard, P., Herbillon, J. (1983). Infrared studies of Ni-bearing clay minerals of the kerolite-
927 pimelite series. Clays and Clay Minerals, 31, 143-151
928 Gleeson,_S.A.,_Butt, C.R.M., Elias, M. (2003). Nickel laterites, a review. SEG Newsletter,
929 54, 11-18.
930 Golightly, J.P., Arancibia, O.N. (1979) The chemical composition and infrared spectrum of
931 nickel- and iron-substituted serpentine from a nickeliferous laterite profile, Soroako,
932 Indonesia. Canadian Mineralogist, 17, 719-728

933 Grazulis, S., Chateigner, D., Downs, R. T., Yokochi, A. T., Quiros, M., Lutterotti, L.,
934 Manakova, E., Butkus, J., Moeck, P. & Le Bail, A. (2009). Crystallography Open Database
935 – an open-access collection of crystal structures. Journal of Applied Crystallography. 42**,**
936 726-729. doi: 10.1107/S0021889809016690
937 Gražulis, S., Daškevič, A., Merkys, A., Chateigner, D., Lutterotti, L., Quirós, M.,
938 Serebryanaya, N. R., Moeck, P., Downs, R. T. & LeBail, A. (2012). Crystallography Open
939 Database (COD): an open-access collection of crystal structures and platform for world-
940 wide collaboration. Nucleic Acids Research 40, D420-D427. doi: 10.1093/nar/gkr900
941 Groppo, C., Rinaudo, C., Cairo, S., Gastaldi, D., Compagnoni, R. (2006). Micro-Raman
942 spectroscopy for a quick and reliable identification of serpentine minerals from
943 ultramafics. European Journal of Mineralogy, 18, 319-329
944 Hofmeister, A.M., Bowey, J.E. (2006). Quantitative infrared spectra of hydrosilicates and
945 related minerals. Monthly Notices of the Royal Astronomical Society, 367, 577-591
946 Hojati, S., Khademi, H. (2013). Thermal behavior of a natural sepiolite from northeastern
947 Iran. Journal of Sciences, Islamic Republic of Iran, 24, 129-134.
948 Hövelmann, J., Putnis, A., Geisler, T., Schmidt, B.C., Golla-Schindler, U. (2010). The
949 replacement of plagioclase feldspars by albite: observations from hydrothermal
950 experiments. Contributions to Mineralogy and Petrology, 159, 43-59.
951 Ishida, K. (1990). Identification of infrared OH librational bands of talc-willemseite solid-
952 solutions and $Al^{(IV)}$-free amphiboles trough deuteration. Mineralogical Journal, 15, 93-104.
953 Jovanoski, G., Makreski, P. (2016). Minerals from Macedonia. XXX. Complementary use of
954 vibrational spectroscopy and X-ray powder diffraction for spectra-structural study of some
955 cyclo-, phyllo- and tectosilicate minerals. A review. Macedonian Journal of Chemistry and
956 Chemical Engineering, 35, 125-155

957 Kaya, S, Topkaya, Y.A.: Chapter 11-Extraction Behavior of Scandium from a refractory
958 nickel laterite ore during the pressur acid leaching process. Rare Earths Industry, 2016,
959 171-182.
960 Lazarevic, S., Jankovic-Castvan, I., Jovanovic, D., Milonjic, S., Janackovic, D.? Petrovic, R.
961 (2007). Adsorption of Pb^{2+}, Cd^{2+} and Sr^{2+} ions onto natural and acid-activated sepiolites.
962 Applied Clay Science, 37, 47-57.
963 Liang, Y., Miranda, C.R., Scandolo, S. (2006). Infrared and Raman spectra of silica
964 polymorphs from an ab initio parametrized polarizable force field. The Journal of
965 Chemical Physics, 125, Article Number 194524
966 Majumdar, A.S., King, H.E., John, T., Kusebauch, C., Putnis, A. (2014). Pseudomorphic
967 replacement of diopside during interaction with (Ni, Mg)Cl2 aqueous solutions:
968 Implications for the Ni-enrichment mechanism in talc- and serpentine-type phases.
969 Chemical Geology, 380, 27-40.
970 Manceau, A., Calas, G., Decarreau, A. (1985) Nickel-bearing clay minerals: I. Optical
971 spectroscopic study of nickel crystal chemistry. Clay Minerals, 20, 367-387.
972 Mano, E.S., Caner, L., Petit, S., Chaves, A.P., Mexias, A.S. (2014). Mineralogical
973 characterization of Ni-bearing smectites from Niquelandia, Brazil. Clays and Clay
974 Minerals, V. 62, 4, 324-335
975 Marsch, E. and Anderson, E. (2011). Ni-Co Laterites-A Deposit Model. USGS Survey Open
976 file Report 2011-1259, 9p
977 Martin de Vidales, J.L., Pozo, M., Alia, J.M., Garcia-Navarro, F., Rull, F. (1991) Kerolite-
978 stevensite mixed layers from the Madrid basin, central Spain. Clay Minerals, 26, 329-342
979 McKeown, D.A., Post, J.E., Etz, E.S. (2002). Vibrational analysis of palygorskite and
980 sepiolite. Clays and Clay Minerals, 50, 666-679.

McRae, M.E. (2021). Nickel statistics and information. U.S. Geological Survey, Mineral Commodity Summaries.

Niedermeir, D.R.D., Putnis, A., Geisler, T., Golla-Schindler, U., Putnis, C.V. (2009). The mechanism of cation and oxygen isotope exchange in alkali feldspars under hydrothermal conditions. Contributions to Mineralogy and Petrology, 157, 65-76.

Orberger, B. (2019): Sonic drilling for rapid vectoring high-quality alluvial diamond deposits. Coring Magazine, June, Issue 10, 28-34.

Orberger, B., van der Ent, A. (2019). Nickel laterites as sources of nickel, cobalt and scandium: Increasing resource efficiency through new geochemical and biological insights. Journal of Geochemical Exploration 204 (2019) 297 – 299; https://doi.org/10.1016/j.gexplo.2019.06.004

Pelletier, B. (1983). Localisation du nickel dans les minéraux garniéritiques de Nouvelle Calédonie. Sciences Géologiques, bulletins et mémoires, 73(1),173-183.

Petriglieri, J.R., Salvioli-Mariani, E., Mantovani, L., Tribaudino, M., Lottici, P.P., Laporte-Magoni, C., Bersani, D. (2015) Micro-Raman mapping of the polymorhs of serpentine. Journal of Raman Spectroscopy, 46, 953-958

Pouchou, J.L., Pichoir, F. (1984). Un nouveau modèle de calcul pour la microanalyse quantitative par spectrométrie de rayons X – Partie I : application à l'analyse d'échantillons homogènes. La Recherche Aérospatiale, 3, 167-192.

Putnis, A. (2009). Mineral replacement reactions. Reviews in Mineralogy and Geochemistry, 70, 87-124.

Putnis, C.V., Geisler, T., Schmid-Beurmann, P., Stephan, T., Giampaolo, C. (2007). An experimental study of the replacement of leucite by analcime. American Mineralogist, 92, 19-26.

1005 Putzolu, F., Balassone, G., Boni, M., Maczurad, M.,Mondillo, N., Najorka, J., and Pirajno, F.
1006 (2018). Mineralogical association and Ni-Co deportment in the Wingellina oxide-type
1007 laterite deposit (Western Australia). Ore Geology Reviews, 97, 21-34. DOI:
1008 https://doi.org/10.1016/j.oregeorev.2018.05.005.
1009 Putzolu, F., Boni, M., Mondillo, N., Maczurad, M., and Pirajno, F. (2019). Ni-Co enrichment
1010 and High-Tech metals geochemistry in the Wingellina Ni-Co oxide-type laterite deposit
1011 (Western Australia). Journal of Geochemical Exploration, 196, 282-296. DOI:
1012 https://doi.org/10.1016/j.gexplo.2018.11.004.
1013 Putzolu, F., Abad, I., Balassone, G., Boni, M., and Mondillo, N. (2020). Ni-bearing smectites
1014 in the Wingellina laterite deposit (Western Australia) at nanoscale: TEM-HRTEM
1015 evidences of the formation mechanisms. Applied Clay Science, 196, 105753. DOI:
1016 https://doi.org/10.1016/j.clay.2020.105753.
1017 Putzolu, F., Santoro, L., Porto, C., Mondillo, M., Machado, M., Saar De Almeida, B., Bastos,
1018 A., and Herrington, R. (2021). The influence of the magmatic to post-magmatic evolution of
1019 the parent rock on the Co deportment in lateritic systems: the example of the Santa Fe' Ni-Co
1020 deposit (Brazil). Economic Geology. DOI: https://doi.org/10.5382/econgeo.4819
1021 Rinaudo, C., Gastaldi, D., Belluso, E. (2003). Charaterization of chrysotile, antigorite and
1022 lizardite by FT-Raman spectroscopy. The Canadian Mineralogist, 41, 883-890
1023 Rosasco, G.J., Blaha, J.J. (1980). Raman microprobe spectra and vibrational mode
1024 assignments of talc. Applied Spectroscopy, 34, 140-144
1025
1026 Savitzky, A., Golay, M.J.E. (1964). Smoothing and differentiation of data by simplified least
1027 squares procedure. Analytical Chemistry, 36, 1627-1639
1028 Secci, M., Zanatta, M., Borovin, E., Bortolotti, M., Kumar, A., Giariola, M., Sanson, A.,
1029 Orberger, B., Daldasso, N., Gialanella, S., Mariotto, G., Montagna, M., Lutterotti, L.

(2018). Mineralogical investigations using XRD, XRF and Raman Spectroscopy in a combined approach. Journal of Raman Spectroscopy. Doi: 10.1002/jrs.5386.

Sharma, S.K., Chio, C.H., Deb, P., Lucey, P.G., Domergue-Schmidt, N., Horton, K.A. (2000). Effect of grain size and grain orientation on the Raman spectra of minerals. 31st Annual Lunar and Planetary Science Conference, Houston, TX, 13-17 March, 2000, 2030 p.

Suarez, M., Garcia-Romero, E. (2006). FTIR spectroscopic study of palygorskite : Influence of the composition of the octahedral sheet. Applied Clay Science, 31, 154-163

Tarling, M.S., Rooney, J.S., Viti, C., Smith, S.A.F., Gordon, K.C. (2018). Distinguishing the Raman spectrum of polygonal serpentine. Journal of Raman Spectroscopy, 49, 1978-1984

Tauler, E., Proenza, J.A., Gali, S., Lewis, J.F., Labrador, M., Garcia-Romero, E., Suarez, M., Long, F., Bloise, G. (2009). Ni-sepiolite-falcondoite in garnierite mineralization from the Falcondo Ni-laterite deposit, Dominican Republic. Clay Minerals, 44, 435-454

Tauler, E., Lewis, J. F., Villanova-de-Benavent, C., Aiglsperger, T., Proenza, J. A., Doménech, C., Gallardo, T., Longo, F., and Gal., S. (2017). Discovery of Ni-smectite-rich saprolite at Loma Ortega, Falcondo mining district (Dominican Republic): geochemistry and mineralogy of an unusual case of “hybrid hydrous Mg silicate–clay silicate” type Ni-laterite. Mineralium Deposita, 52(7), 1011-1030.

Teitler, Y., Cathelineau, M., Ulrich, M., Ambrosi, J. P., Munoz, M., and Sevin, B. (2019). Petrology and geochemistry of scandium in New Caledonian Ni-Co laterites. Journal of Geochemical Exploration, 196, 131-155.

Villanova-de-Benavent, C., Proenza, J.A., Gali, S., Garcia-Gasco, A., Tauler, E., Lewis, J.F., Longo, F. (2014). Garnierites and garnierites: Textures, mineralogy and geochemistry of garnierites in the Falcondo Ni-laterite deposit, Dominican Republic. Ore Geology Reviews, 58, 91-100

1055 Villanova-de-Benavent, C., Nieto, F., Viti, C., Proenza, J.A., Gali, S., Roqué-Rosell, J.
1056 (2016). Ni-phyllosilicates (garnierites) from the Falcond Ni-laterite deposit (Dominican
1057 Republic): Mineralogy, nanotextures, and formation mechanisms by HRTEM and AEM.
1058 American Mineralogist. 101, 1460-1473
1059 Villanova-de-Benavent, C., Jawhari, T., Roqué-Rosell, J., Gali, S., Proenza, J.A. (2019). Ni-
1060 bearing phyllosilicates ("garnierites"): New insights from thermal analysis, μRaman and
1061 IR spectroscopy. Applied Clay Science, 175, 47-66
1062 Wang, A., Freeman, J.J., Jolliff, B.L. (2015). Understanding the Raman spectral features of
1063 phyllosilicates. Journal of Raman Spectroscopy, 46, 829-845
1064 Wells, M.A, Ramanaidou, E.R.; Verrall, M., Tessarolo, C. (2009). Mineralogy and crystal
1065 chemistry of ''garnierites''in the Goro lateritic nickel deposit, New Caledonia. Eur. J.
1066 Min., 21, 467-483.
1067 Wilkins, R.W.T., Ito, J. (1967). Infrared spectra of some synthetic talcs. American
1068 Mineralogist, 52, 1649-1661.
1069 Williams-Jones, A.E. & Vasyukova, O.V. (2018). The Economic Geology of Scandium, the
1070 Runt of the Rare Earth Element Litter. Economic Geology, 113, 4, 973-988.
1071 Yariv, S., Heller-Kallai, L. (1975). The relationship between the I.R. spectra of serpentines
1072 and their structures. Clays and Clay Minerals, 23, 145-152
1073 Yeniyol, M. (2014). Characterization of two forms of sepiolite and related Mg-rich clay
1074 minerals from Yenidog an (Sivrihisar, Turkey). Clay Minerals, 49, 91-108
1075 Yongue-Fouateu, R., Ghogomu, R.T., Penaye, J., Ekodeck, G.E.,Stendal, H., Colin, F. (2006).
1076 Nickel and cobalt distribution in the laterites of the Lomié region, south-east Cameroon.
1077 Journal of African Earth Sciences. 45, 33-47.